Chapter 2

Rare Earth-Doped Anatase TiO_2 Nanoparticles

Vesna Đorđević, Bojana Milićević and

Miroslav D. Dramićanin

Additional information is available at the end of the chapter

http://dx.doi.org/10.5772/intechopen.68882

Abstract

Titanium dioxide is a wide band-gap semiconductor of high chemical stability, nontoxicity and large refractive index. Because of the high photocatalytic activity, anatase is a preferred TiO_2 form in many applications such as for air and water splitting and purification. Doping of TiO_2 with various ions can increase the photocatalytic activity by enhancing light absorption in visible region and can alter structure, surface area and morphology. Also, by doping TiO_2 with optically active ions, visible light via up- or downconversion luminescence can be produced. It is a challenge to optimize the synthesis procedure to incorporate rare earth RE^{3+} ions into the TiO_2 structure due to large mismatch in ionic radii between the Ti^{4+} and RE^{3+} and because of the charge imbalance. Visible (VIS) and ultraviolet (UV) luminescence of several RE^{3+} ions can be obtained when incorporated into anatase TiO_2, also affecting microstructural characteristics of TiO_2. It is of great importance to summarize publications on rare earth-doped anatase TiO_2 nanoparticles to find correct TiO_2-RE combination to sensitize trivalent rare earths luminescence, as well as to predict or tune structural and morphological properties. A better understanding on these topics may progress the desired design of this kind of material towards specific applications.

Keywords: anatase, rare earth ions, photoluminescence, photocatalysis

1. Introduction

Rare earth (RE) elements are sixth period elements in the periodic table, from ^{57}La to ^{71}Lu. Because of many similarities, such as ionic +3 charges and similar ionic radius, ^{39}Y that also belongs to the III transition group and is positioned just above ^{57}La is also often considered

as a part of the RE group. Even though the group is regarded as rare earth elements, they are not particularly rare. However, they are costly but highly efficient for many technological applications, mainly in lighting and display devices. With the absence of ^{57}La and ^{71}Lu, RE atoms, all have incompletely filled 4f orbitals that are positioned in the inner shell of xenon [Xe: $1s^2\ 2s^2\ 2p^6\ 3s^2\ 3p^6\ 4s^2\ 3d^{10}\ 4p^6\ 5s^2\ 4d^{10}\ 5p^6$] electron configuration, which are responsible for their emission properties. Since they are shielded by outer $5s^2$ and $5p^6$ orbitals, electrons from 4f orbitals do not participate in bonding and are only slightly affected by the surroundings of the ions. Ionic +3 charges are the most often, although some cases +2 and +4 can be stable as presented in **Table 1**. Electronic states are noted as $^{2S+1}L_J$, where L is the orbital angular momentum, S is the spin angular momentum, and J is the total angular momentum, and corresponding notations are also presented in **Table 1**. Lanthanide contraction makes significant decrease of ionic radii in the series with an increase in atomic number, and the values for six-coordinated RE^{3+} are also presented in **Table 1**.

Laporte's selection rule states that electron transitions between 4f states are forbidden, but they become partially allowed when RE ions are incorporated in non-symmetric sites [2, 3]. In that way, each ion has characteristic 4f energy levels with narrow-emission lines that depend on the crystalline environment of the host material in the order of few hundred cm^{-1}. The Dieke diagram is the energy-level diagram of trivalent lanthanide 4f electrons of RE^{3+}

Atomic number	Name	RE symbol	Atom	RE^{2+}	RE^{3+}	RE^{4+}	$^{2S+1}L_J$	Radii RE^{3+}_{VI} [Å]
57	Lanthanum	La	$5d^1\ 6s^2$	–	[Xe]	–	$^1S_0$	1.032
58	Cerium	Ce	$4f^1\ 5d^1\ 6s^2$	–	$4f^1$	[Xe]	$^2F_{5/2}$	1.020
59	Praseodymium	Pr	$4f^3\ 6s^2$	–	$4f^2$	$4f^1$	$^3H_4$	0.990
60	Neodymium	Nd	$4f^4\ 6s^2$	$4f^4$	$4f^3$	$4f^2$	$^4I_{9/2}$	0.983
61	Promethium	Pm	$4f^4\ 6s^2$	–	$4f^4$	–	$^5I_4$	0.970
62	Samarium	Sm	$4f^6\ 6s^2$	$4f^6$	$4f^5$	–	$^6H_{5/2}$	0.958
63	Europium	Eu	$4f^7\ 6s^2$	$4f^7$	$4f^6$	–	$^7F_0$	0.947
64	Gadolinium	Gd	$4f^7\ 5d^1\ 6s^2$	–	$4f^7$	–	$^8S_{7/2}$	0.938
65	Terbium	Tb	$4f^9\ 6s^2$	–	$4f^8$	$4f^7$	$^7F_6$	0.923
66	Dysprosium	Dy	$4f^{10}\ 6s^2$	–	$4f^9$	$4f^8$	$^{11}H_{15/2}$	0.912
67	Holmium	Ho	$4f^{11}\ 6s^2$	–	$4f^{10}$	–	$^5I_8$	0.901
68	Erbium	Er	$4f^{12}\ 6s^2$	–	$4f^{11}$	–	$^4I_{15/2}$	0.890
69	Thulium	Tm	$4f^{13}\ 6s^2$	$4f^{13}$	$4f^{12}$	–	$^3H_6$	0.880
70	Ytterbium	Yb	$4f^{14}\ 6s^2$	$4f^{14}$	$4f^{13}$	–	$^2F_{7/2}$	0.868
71	Lutetium	Lu	$4f^{14}\ 5d^1\ 6s^2$	–	$4f^{14}$	–	$^1S_0$	0.861

Table 1. Outer electronic configurations of RE atoms and ions, outside of the [Xe] shell, ground-state term of RE^{3+} and radii of 6-coordinated RE^{3+} (taken from Ref. [1]).

incorporated in $LaCl_3$ crystals, which can be found in the original or revised form, which is informative for many materials [4–7]. It schematically represents variations between ground- and excited-level energies or rare earth ions, proposing emissions of almost any colour in visible spectra by using one, or a combination of various RE ions in hosts.

Luminescent materials that absorb energy as light and do not emit it as heat, but as ultraviolet, visible or infrared (IR) light, are called phosphor materials. Typically, they are composed of insulating or semiconducting host material that is doped with activator ions. Phosphors with RE ions as activators are important materials that have found applications in artificial light, cathode-ray tubes, vacuum fluorescent and field emission displays, solid-state lasers, and so on [8]. It is now a custom to refer materials that have at least one dimension less than 100 nm as nanomaterials. The great number of atoms in top layers of nanoparticles significantly alters their optical properties; hence, it is justified to name nanostructured phosphors as a nanophosphors. Today, nanophosphors can be found in many forms, such as nanopowders, composites, coatings and thin films, giving new possibilities for application in bio-imaging and various types of physical and chemical sensing [9–11].

Photoluminescence of RE ions can be induced by the absorption of light through host lattice (host, H) that is transferred to RE ion (activator, A), directly exciting A, or energy transfer from other exited ions (sensitizer, S) that are also incorporated in matrix. A schematic diagram showing direct and indirect excitations with energy transfer resulting in the emission of light or heat is presented in **Figure 1(a)**.

When RE ions are used as activators in phosphor materials, depending on the positions of energy levels in RE ion, two main energy conversion mechanisms can lead to radiative energy transfer that results in the emission of light, one being downconversion, and the other upconversion. As it can be seen in **Figure 1(b)**, the principal difference between the two is the difference in excited and emitted energies. As schematically presented, in downconversion process electrons are excited by higher-energy photons compared to energy obtained from emission. In the process, prior to the emission of photons some energy is lost by non-radiative transitions. Oppositely, in upconversion process electrons are excited by lower-energy photons compared to energy obtained from emission. In order to preserve energy conservation rule, more than one photon is necessary for either single-ion excited-state absorption process, or in energy transfer upconversion process where the second ion is the sensitizer ion.

In order to fully understand the processes of downconversion light emission, we refer to energy-level diagram scheme presented in **Figure 2**. In honour of professor Alexander Jablonski, this type of energy diagrams is often called the Jablonski diagram. It qualitatively represents electronic energy levels as bolded horizontal lines and vibrational energy levels as a stack of horizontal lines in vertical energy diagram. Straight and wavy vertical arrows represent transitions between the states, where straight arrow represents transition associated with photon, while wavy arrows represent non-radiative transfers. A radiative decay process is a process in which electron releases some of its excitation energy as photon, while in a non-radiative decay excess energy is transferred into thermal motions, as vibration, rotation and translation processes, heat. Once an electron is excited through very quick process of absorption of photon, into, for example, some vibronic state of second excited singlet state, there

are several ways that energy may be dissipated. The first is through vibrational relaxation, a non-radiative process that lowers energy of electron to the lowest excited singlet state, with or without non-radiative internal conversion process, depending on the overlap of vibrational and electronic energy of different states. Next, a radiative process of energy transfer to ground singlet state is followed by emission of photons in terms of fluorescence. There is no change in multiplicity $S_1 \rightarrow S_0$, so the transition is spin allowed and consequently fast. Since there are a large number of vibrational levels in electronic states, transitions can result in a range of emitted wavelengths. There is also a probability of non-radiative relaxations between

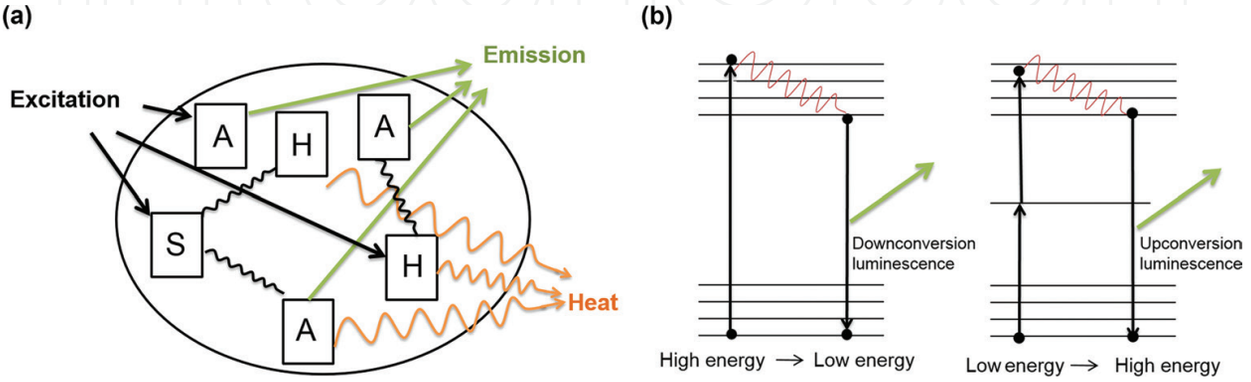

Figure 1. (a) Direct and indirect excitation with energy transfer resulting in emission of light or heat, by activators (A), hosts (H) and sensitizers (S). (b) Basic mechanisms of downconversion and upconversion luminescence.

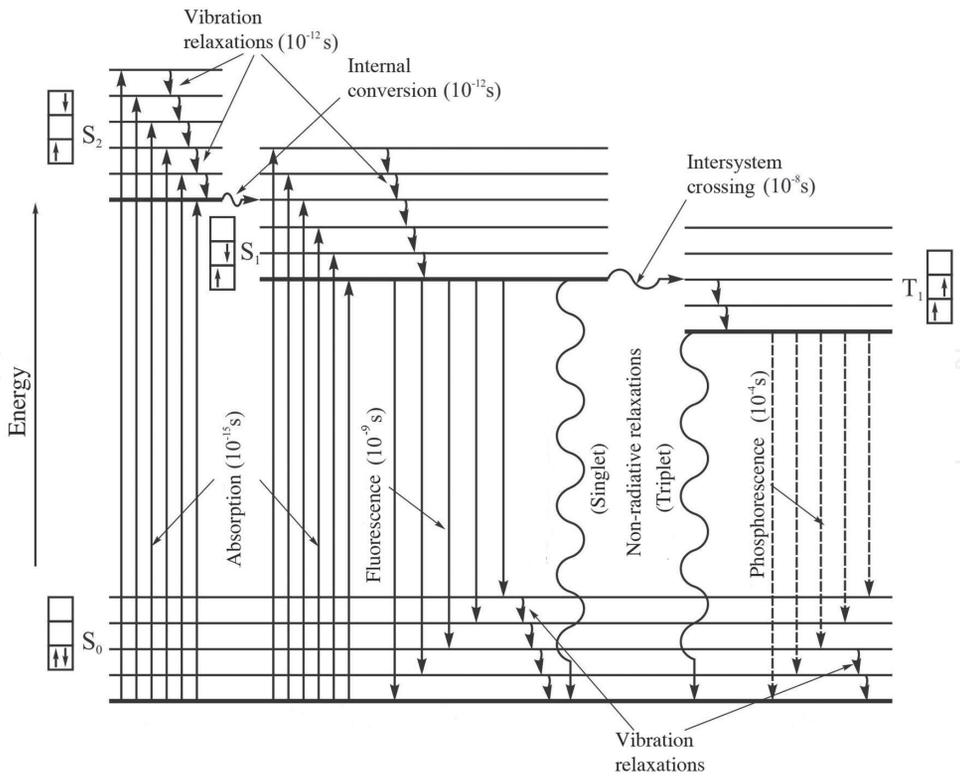

Figure 2. Radiative and non-radiative processes with corresponding approximate time interval of the processes in energy-level diagram scheme. S_0, ground singlet state; S_1, S_2, excited singlet states; T_1, excited triplet state.

the singlet states ($S_1 \rightsquigarrow S_0$). If in the process of dissipating of energy spin multiplicity changes by slower process of intersystem crossing, energy can be radiatively emitted from lowest excited triplet state to ground singlet state by phosphorescence $T_1 \rightarrow S_0$, or non-radiatively by relaxations between the triplet and singlet states ($T_1 \rightsquigarrow S_0$). Intersystem crossing and therefore phosphorescence are spin-forbidden processes; nevertheless, by coupling vibrational factors into the selection rules transitions become partially allowed, and they are consequently much slower.

2. Synthesis of rare earth-doped anatase TiO_2 nanoparticles

TiO_2 nanoparticles present several advantages for applications compared to their bulk counterparts. Their high-surface-to-volume ratio, improved charge transport and lifetime, afforded by their dimensional anisotropy, allows efficient contribution to the separation of photo-generated holes and electrons [12]. The properties of TiO_2 depend on its crystal structure, surface chemistry, dopants, doping levels, crystallization degree, size and morphology [13]. Hence, it is of great importance to control the particle size, shape and distribution of the synthetized TiO_2. To achieve desired characteristics, a variety of TiO_2 nanostructures have been prepared, such as nanoparticles, nanotubes, nanorods, nanofibres, nanosheets and nanofilms. These structures can be synthetized through various preparation methods, such as sol-gel, direct oxidation, micelle and inverse micelle techniques, sonochemical, hydrothermal/solvothermal, microwave, chemical vapour deposition, physical vapour deposition and electrospray deposition [14–17]. Significant progress has been made in the last 10 years regarding new approaches to the preparation of TiO_2. These include doping TiO_2 with optically active rare earth ions (RE). TiO_2 can be considered as an 'unusual' matrix for doping with RE^{3+} ions due to the large mismatch of both charge and ionic radius between the dopant and the host constituent cations. It is a challenge even now to optimize the synthesis procedure in the way to efficiently incorporate RE^{3+} ions into TiO_2 nanostructure and to obtain material with high crystallinity. Spectroscopic studies have showed that the RE ions can reside in the anatase in three different sites [18–20]. In nanopowders, substantial number of RE ions occupies the sites near the surface with the lowest point symmetry.

TiO_2 occurs in three most abundant crystalline phases in nature: anatase (tetragonal), rutile (tetragonal) and brookite (orthorhombic). Rutile TiO_2 is the most stable form, while anatase and brookite phases are metastable and can be transformed to rutile phase at higher temperatures. Even though rutile is denser and thermodynamically more stable than anatase, this significant temperature treatment is not favourable for the formation of nanoparticles with a diameter lower than 15 nm, which is a feature of anatase form TiO_2 [21, 22].

Sol-gel synthesis is the most common method for the preparation of RE-doped TiO_2 nanoparticles, being simple, cost-effective and low-temperature procedure, with the ability to fabricate nanostructure with high purity, homogeneity and controllable morphology. This synthesis includes the process of hydrolysis and poly-condensation of Ti–OH–Ti or Ti–O–Ti bonds forming densely three-dimensional structure that after heating changes from sol to gel, and after thermic treatment results in the form of oxide. Titanium source precursors can

be alkoxides (such as titanium (IV)-isopropoxide (TTIP), titanium (IV)-butoxide (TBT)) or titanium (IV)-chloride ($TiCl_4$). RE ion precursors can be acid-soluble oxides (RE_2O_3) or water-soluble nitrates, acetates or chlorides ($RE(NO_3)_3{\cdot}xH_2O$, $RE(CH_3COO)_3{\cdot}x(H_2O)$, $RECl_3$).

In the method of hydrolysis of TTIP, products are characterized by low surface area, wide pore size distribution with contribution to pores of mesopores scale (<50 nm) [22]. The sol-gel synthesis with a two-step procedure of mixing precursor solutions was successfully used to obtain RE-doped TiO_2 [18, 23–36]. The gels obtained in such procedures undergo various temperature treatments, which are summarized in **Table 2**. In the method of hydrolysis of $TiCl_4$, which is another sol-gel method for the preparation of RE-doped anatase TiO_2, minor amounts of brookite phases are often present and slightly larger crystallite size compared to RE-doped TiO_2 from the titanium alkoxides is reported [13, 37].

Hydrothermal synthesis is a heterogeneous chemical reaction in the presence of an aqueous solvent, above room temperature (<200°C) in a closed system, where the pressure is elevated.

Dopant ions	Doping conc. (%)	Calcination temperature (°C)	Crystalline phase	Crystallite size* (nm)	BET surface area (m^2/g)	Pore diameter (nm)	Refs.
–	–	400–700	A	8.14–79.1	25–117	3.26–6.4	[13, 18, 22–28, 38, 39]
–	–	500–800	A + R	14.1–101.8	0.59–17.94	4.68	[22–24, 29]
–	–	800–1000	R	32.7–100	0.34–16.7	–	[22–24]
Sc	2	500	A + B	16.6	–	–	[37]
Sc	2	500–550	A	16.6–26.9	–	–	[13]
Sc	2	600	A + R	45.0	–	–	[13]
Sc	2	650–800	R	51.7–65.2	–	–	[13]
Y	0.25–2	400–500	A	8.5–9.4	89.68–151	–	[28, 30, 31]
La	0.1–10	500	A	8.57–13.40	46.51–105.66	4.90–12.34	[25]
La	–	600	A + R	17.2	36.7	–	[32]
Ce	0.1–10	500	A	8.68–13.79	53.31–94.49	5.46–12.52	[24, 25]
Ce	5	800	A + CeO_2	–	–	–	[24]
Pr	0.25–1	400–650	A	9–20	77.5–134	–	[28, 33, 40]
Nd	0.05–4	400–700	A	10–20	7.5–75	–	[24, 34, 40, 41]
Nd	0.1–5	800	A + R	25	<1.0	–	[24, 41]
Nd	0.1–5	900–1000	A + R + $Nd_4Ti_9O_{24}$	–	–	–	[24]
Sm	0.3–3	420–700	A	5.8–12	50.78–95.9	5.20	[18, 29, 34, 35, 38, 42]
Sm	0.3–0.5	800	A + R	–	16.1–24.7	–	[38]

Dopant ions	Doping conc. (%)	Calcination temperature (°C)	Crystalline phase	Crystallite size* (nm)	BET surface area (m^2/g)	Pore diameter (nm)	Refs.
Eu	0.25–3	400–500	A	6–12	88.55–178.3	3.6–7.5	[18, 27–30, 39, 42]
Eu	5	800	A + R	27	–	–	[24]
Gd	1–2	500–700	A	6.9–15.1	32.8–97.7	–	[22]
Gd	2	800	A + $Gd_2Ti_2O_7$	–	–	–	[22]
Gd	5	600–800	A + R	26–27	–	–	[24, 32]
Gd	5–10	800–900	A + R + $Gd_2Ti_2O_7$	7.2–14.7	15.3–51.5	–	[22]
Tb	0.7–3	420–500	A	8.69–9	88.34	5.43	[18, 29]
Tb	5	800	A + R	25.5	–	–	[24]
Dy	0.3	450–650	A	9–31	60.4–80.6	–	[33]
Dy	5	800	A + R	24	–	–	[24]
Ho	0.3–2	500–800	A	12.5–20.5	76.76–98.81	–	[23, 36]
Er	0.25–5	400–700	A	8.5–21.9	18–132	–	[24, 26, 28, 42]
Er	5	800	A + $Er_2Ti_2O_7$	23.8	–	–	[24]
Yb	0.21–1.13	500	A	–	–	–	[43]
Yb	5	600–800	A + R	19–23	–	–	[24, 32]

*Anatase phase.

Table 2. The sol-gel synthesis conditions and major physicochemical properties of RE-doped TiO_2 nanostructures; A-anatase, B-brookite, R-rutile.

The synthesis has been used to produce homogeneous, high-purity, crystalline nanostructured RE-doped TiO_2 with different morphologies: nanotubes, nanobelts, nanowires or spherical nanoparticles. Alkoxide Ti precursors and water-soluble RE precursors are activated by acids or bases prior to the temperature treatments in Teflon-liners autoclave up to several days [28, 44–53]. Obtained precipitates should be washed to neutral pH [47] before calcination in order to gain well-defined TiO_2 nanoparticles. Also, hydrothermal route can use the synthesized or commercial available TiO_2 nanoparticle without the post-calcination treatment [44, 46]. The main difference of *solvothermal* synthesis is using other solvents than water. The obtained samples are spherical nanoparticles with an average diameter of 16 nm and the doping process can be easily achieved without significant loss of dopants [54]. The main characteristics and major physicochemical properties of RE-doped TiO_2 nanostructures synthetized by hydrothermal and solvothermal are summarized in **Table 3**.

Electrospinning method can be employed to produce nanostructure RE-doped TiO_2 with fibre morphology and the average fibre diameter in the range of 35–80 nm. Typically, RE-doped TiO_2

Dopant ions	Doping conc. (%)	Hydrothermal treatment (°C)	Calcination temperature (°C)	Crystalline phase	Crystallite size (nm)	BET surface area (m^2/g)	Morphology	Refs.
–	–	140–160	≤400	A	9.3–30	102–312.5	Spherical particle (d^* = 10–30 nm)	[28, 47–49, 54]
–	–	200	500	A + R	22.8	53–165	Spherical particle	[44, 51]
Y	0.25	150–160	≤400	A	9.8	120–157	Spherical particle (d = 5–15 nm)	[28, 47]
Y	0.3	80	–	A + R	–	–	–	[51]
La	0.11–0.53	200	500	A + R	22.32–24.38	69–86	Spherical particle	[44]
La	0.3	80	–	A + R	–	–	–	[51]
Pr	0.25–2.0	100	400	A	5.04–6.22	155–170	Spherical particle (d < 10 nm)	[55]
Pr	0.25	160	400	A	9.0	127	Spherical particle (d = 5–15 nm)	[28]
Pr	0.3	80	–	A + R	–	200	–	[51]
Nd	0.3	80	–	A + R	–	220	–	[51]
Sm	1	150	500	A	16	–	Spherical particles ($d \sim$ 16 nm)	[54]
Eu	0.25–0.5	130–200	400–500	A	8.6	133	Spherical particle (d = 5–15 nm)	[28, 56]
							Sub-microspheres (d = 300 nm)	[52]
							Spindle particles (d = 50–100 nm, l^* = up to several μm)	[53]
							Nanorods (d = 10–20 nm, l = up to several μm)	[53]
							Nanobelts (w^* = 200–400 nm, l = several μm)	[45]

Dopant ions	Doping conc. (%)	Hydrothermal treatment (°C)	Calcination temperature (°C)	Crystalline phase	Crystallite size (nm)	BET surface area (m^2/g)	Morphology	Refs.
Eu	–	180	700	A + R	–	–	Nano-belts forming aggregates (d = 50–200 nm)	[45]
Eu	–	180	900	R	–	–	Nano-belts forming aggregates (d = 50–200 nm)	[45]
Eu	1	150	500	A	16	–	Spherical particle ($d \sim$ 16 nm)	[54]
Ho	0.75	150**	–	A + R	7.6–20.4	–	Nanowires (d = 500 nm, l = 15 nm)	[46]
2% Ho + Yb	2% Yb	120**	25, 100, 280	A	–	–	Nanotube	[50]
Er	0.25–4	140–160	>400	A	8.9–16	98.1–127	Spherical particles ($d <$ 16 nm)	[28, 48, 49, 54]

*d, diameter; w, weight; l, length.

**TiO_2 calcined at 550°C was used in the synthesis route.

Table 3. Hydrothermal and solvothermal synthesis conditions and major physicochemical properties of RE-doped TiO_2 nanostructures.

http://dx.doi.org/10.5772/intechopen.68882

nanofibres are fabricated with the use of polymer solvents of polyvinyl pyrrolidone (PVP) or polyvinyl alcohol (PVA), titanium alkoxides and RE chlorides or nitrates. Starting solutions in glass syringe with stainless-steel needle are connected to a high voltage and electrospun in air at different tensions, needle-target distances and feed rates [57–61]. In order to remove the polymeric component and obtain nanocrystalline anatase, RE-doped TiO_2, as-spun nanofibres were calcined at 500°C. However, the pure phase of RE-doped rutile TiO_2 can be obtained after higher calcination temperature (>1000°C). The synthesis conditions and major physicochemical properties of RE-doped TiO_2 nanostructures reported in the literature are summarized in **Table 4**.

Precursor materials	Dopant ions	Doping conc. (%)	Calcination temperature (°C)	Crystalline phase	Crystallite size (nm)	Fibre diameter (nm)	Refs.
PVP, TTIP	–	–	400–500	A			[57, 58]
PVP, TTIP	–	–	500–900	A + R	15.71–40		[57–59]
PVP, TTIP	–	–	1000	R			[57]
PVP, TTIP, $Y(NO_3)_3$	Y	1–2	500	A + R	11.35–13.8		[59]
PVP, TTIP, $Y(NO_3)_3$	Y	3	500	A	8.8		[59]
PVP, TTIP, $La(NO_3)_3$	La	1	500–800	A		40	[57]
PVP, TTIP, $La(NO_3)_3$	La	1	900–1000	A + R			[57]
PVP, TTIP, $La(NO_3)_3$	La	1	1100	R			[57]
PVA, TTIP, $La(NO_3)_3$	La	1	500	A			[58]
PVA, TTIP, $La(NO_3)_3$	La	1	700	A + R	12.51		[58]
PVA,,TTIP, $Ce(NO_3)_3$	Ce	1	500	A			[58]
PVA, TTIP, $Ce(NO_3)_3$	Ce	1	700	A + R	11.49		[58]
PVA, TTIP, $Nd(NO_3)_3$	Nd	1	500	A			[58]
PVA, TTIP, $Nd(NO_3)_3$	Nd	1	700	A + R	10.2		[58]
PVP, TTIP, $Eu(NO_3)_3$	Eu	1, 3	500–800	A		60, 70	[57]
PVP, TTIP, $Eu(NO_3)_3$	Eu	1	900	A + R			[57]
PVP, TTIP, $Eu(NO_3)_3$	Eu	3	900	A + R + $Eu_2Ti_2O_7$			[57]

Precursor materials	Dopant ions	Doping conc. (%)	Calcination temperature (°C)	Crystalline phase	Crystallite size (nm)	Fibre diameter (nm)	Refs.
PVP, TTIP, $Eu(NO_3)_3$	Eu	1, 3	1000–1100	R + $Eu_2Ti_2O_7$			[57]
PVP, TTIP, $Tb(NO_3)_3$	Tb	1, 3	400–800	A		35, 80	[60]
PVP, TTIP, $Tb(NO_3)_3$	Tb	1	900	A + R			[60]
PVP, TTIP, $Tb(NO_3)_3$	Tb	3	900	A + R + $Tb_2Ti_2O_7$			[60]
PVP, TTIP, $Tb(NO_3)_3$	Tb	1, 3	1000–1100	R + $Tb_2Ti_2O_7$			[60]
PVP, TTIP, $Er(NO_3)_3$	Er	1	400–900	A		60	[57]
PVP, TTIP, $Er(NO_3)_3$	Er	1	1000–1100	A + R + $Er_2Ti_2O_7$			[57]
PVP, TTIP, $Er(NO_3)_3$	Er	3	500–800	A		77	[57]
PVP, TTIP, $Er(NO_3)_3$	Er	3	900	A + R + $Er_2Ti_2O_7$			[57]
PVP, TTIP, $Er(NO_3)_3$	Er	3	1000–1100	R + $Er_2Ti_2O_7$			[57]
PVP, TBT, $ErCl_3$	Er	0.5–1.5	500	A	11.5–8.1		[61]
PVP, TBT, $ErCl_3$	Er	0.5	600–700	A + R	17.9–23.1		[61]
PVP, TBT, $ErCl_3$	Er	0.5	800	R	27		[61]
PVP, TTIP, $Yb(NO_3)_3$	Yb	1, 3	400–800	A		55, 70	[60]
PVP, TTIP, $Yb(NO_3)_3$	Yb	1	900	A + R			[60]
PVP, TTIP, $Yb(NO_3)_3$	Yb	3	900	A + R + $Yb_2Ti_2O_7$			[60]
PVP, TTIP, $Yb(NO_3)_3$	Yb	1, 3	1000–1100	R + $Yb_2Ti_2O_7$			[60]

Table 4. The electrospinning synthesis conditions and major physicochemical properties of RE-doped TiO_2 nanostructures.

Thermal plasma pyrolysis is rarely used for the synthesis and preparation of RE-doped TiO_2 nanopowders, which enables highly crystallized and well-dispersed nanoparticles due to the processing temperature (up to 1.0×10^4 K), rapid quenching rate at the plasma tail (~$10^{5–7}$ K/s) and very short residence time [62]. The advantage of this synthesis is

that well-dispersed and highly crystalline nanoparticles in a single processing step are obtained, without post-annealing treatment. On the other hand, it promotes crystallization of several crystalline phases of TiO_2, and with small amount of RE dopants mixtures of anatase and rutile are formed, while at higher temperatures dititanate structures were also formed [62].

Electrochemical synthesis is a significant method in the preparation of TiO_2 nanotubes at substrates, providing the precise control of nanotube morphology, length and pore size, and the formation of thick walls at substrates. Electrolytes used in this procedure are fluorides, where the concentration strongly effects on the dimensions and pH on the thickness of TiO_2 nanotubes [63, 64]. With anodic potential from 10 to 30 V, nanotubes with diameters between 15 and 200 nm are formed, and by cathodic electrochemical process RE ions are incorporated into the nanotubes. Also, magnetron-sputtering method can be used to prepare RE-doped TiO_2 films [65] as well as evaporation-induced self-assembly method [66–69].

In order to investigate structural, morphological, photocatalytic and optical properties of RE-doped anatase TiO_2 nanopowders with a series of RE^{3+} ions (Pr, Nd, Sm, Eu, Dy, Tb, Ho, Er and Tm) at a fixed concentration of 1 at.%, the sol-gel method has been used. To prepare samples, titanium (IV)-isopropoxide, water, ethanol and nitric acid were mixed in 1:3:20:0.08 molar ratios and the synthesis procedure is schematically shown in **Figure 3** and given in Ref. [27].

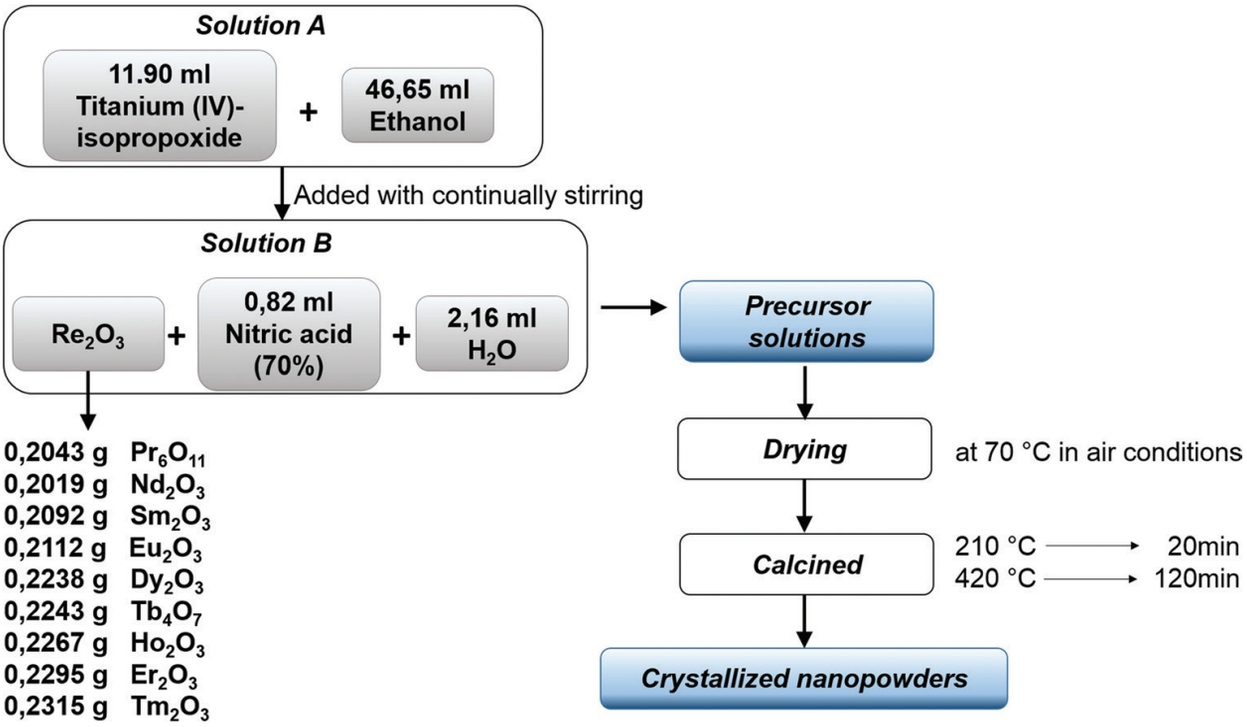

Figure 3. Schematic representation of the sol-gel synthesis with quantities of precursors used to prepare 3 g RE^{3+}-doped TiO_2 nanopowders.

3. The influence of rare earth doping on the stability of phase structure, surface area and morphology of anatase TiO_2 nanoparticles

In most morphologies of calcinated TiO_2 powders, anatase phase is stabile up to temperatures below 500°C. Anatase to rutile crystalline phase transformation occurs above this temperature. In RE ions doped of anatase materials, the temperature of phase transformations shifts to higher values, suggesting the stabilization of anatase phase. As it can be seen in **Tables 2–4** in Section 2, phase transformations of RE-doped anatase to rutile crystalline phase occur in the temperature range of 500–1000°C. There are three types of dominant nucleation modes in forming rutile from anatase, bulk, interface and surface, which lead to the phase transformation. The proposed mechanisms affect the rate of grain forming and the density of rutile nucleation sites. The bulk nucleation of rutile particles is most likely to occur at temperatures above 500°C, when the grain boundary is surrounded by RE ions hindering the surface nucleation. The interface nucleation mode is dominant in the range of 550–680°C, when rutile particles with a larger crystallite size are formed on account of anatase particles, probably through aggregating of some anatase particles at the surfaces [70]. When calcination temperature increases, the phase transformation is not completed because the surface region is still in the mixed phases of anatase and rutile, with increasing percentage of rutile particles. At the same time, the formation of multiphase RE-titanate structures can also be noticed at higher temperatures, usually dititanates pyrochlore structures with a general formula of $RE_2Ti_2O_7$ [22, 57, 60, 71]. The contribution of these structures increases with RE-doping concentration [57], and it is more pronounced with RE ions with smaller ionic radius (heavier ions). When RE ions with a larger ionic radius occupy TiO_2 lattice sites, ionic mobility is hindered and the possibility of forming other titanate phases is lower. The electrospinning sol-gel route can be used to fabricate RE-doped TiO_2 with pure rutile phase at higher calcination temperature (>1000°C) without the formation of the $RE_2Ti_2O_7$ phase [57].

The influence of doping TiO_2 with RE, where larger RE ions of different charge (+3) compared to Ti ions are introduced into the anatase phase, gives rise to substitutional defects and, consequently, the large decrease in the short lattice order, thus in the reduction of the crystallite size. With increasing the concentration of RE ions, amorphization of crystalline powders is expected. The contents of RE ions used in sol-gel synthesis are usually in the 0.1–3% range, while further addition of RE ions (≥5%) effectively obstructs TiO_2 crystallinity owing to a lattice distortion, and remarkably reduces the crystallite size [22, 25]. The increase of doping concentration leads to a higher content of RE–O–Ti bonds that inhibit the growth of TiO_2 crystal grains restricting the direct contact of anatase particles, shifts diffractions to lower 2 theta angles, and as a consequence of smaller crystallites, broadening of X-ray diffraction (XRD) maxima [18, 55, 72, 73]. Even in undoped TiO_2, the anatase phase is reported to be thermodynamically stable at very low particle size. In respect to the particle size, it is reported that rutile phase can be formed when the crystallite size reaches a critical value of 12–20 nm [22]. Therefore, with the temperature increase, the crystallite size increases, which also favours anatase to rutile phase conversion. The influence of the incorporation of RE ions into the TiO_2 is reflected in the reduction of the crystallite size that inhibits the transformation of anatase to rutile phase. Taking into account all possible RE-doping effects on the stability

of anatase phase, size and concentration of RE ion, applied synthesis method and calcination temperature, a number of parameters may be varied in an attempt to optimize desired TiO_2 powder structure and properties.

RE-doped TiO_2 nanopowders were prepared by the sol-gel route using a series of RE (Pr, Nd, Sm, Eu, Dy, Tb, Ho, Er, Tm) oxides and titanium(IV)-isopropoxide. The final calcination treatment is carried out at a temperature of 420°C for 2 h. XRD measurements were done on synthesized powders using Rigaku SmartLab instrument under the Cu $K_{\alpha 1,2}$ radiation, in a 2θ-range from 10° to 120° in 0.02° steps, and are shown in **Figure 4**. The XRD patterns indexed according to the ICDD card No. 00-021-1272. These patterns consist of the characteristic, intense peaks corresponding to 101, 004, 200, 105, 211 and 204 main reflections from anatase phase TiO_2 in all RE-doped TiO_2 nanopowders. There are no diffraction peaks of another crystalline phase of TiO_2 (rutile or brookite), rare earth oxide phase or dititanate pyrochlore structures. The analysis of relevant structural parameters was obtained using PDXL Integrated software, and calculated results are presented in **Table 5**. The average crystallite size of undoped TiO_2 was determined to be 149.6 Å, which is a much higher value than for the doped ones, suggesting the decrease in crystallinity with doping with RE as a result of the RE–O–Ti bonds in doped TiO_2 nanopowders. A consequence of the incorporation of larger RE ion compared to Ti ion ($r(Ti_{VI}^{4+})$ = 0.605 Å into anatase structure results in an increase in cell parameters that result in an increase of cell volume.

Mesoporous materials have important properties for potential applications, such as well-defined pore structure, uniform pores in the range between 2 and 50 nm and high surface area that provides a large number of active sites. Nevertheless, during the calcination treatment, TiO_2 nanoparticles pass through the process of crystal growth and anatase-to-rutile phase transformation causing the collapse of the mesoporous framework and a decrease of surface area. Incorporation of RE ions into the TiO_2 matrix has been presented as a potential strategy to overcome these disadvantages, with a possibility for thermal stability of the mesoporous structure and retarded decreasing of surface area of TiO_2 nanoparticles at high temperatures [25]. Also, RE ion-doped nanocrystalline TiO_2 has a significant number of active sites at anatase wall, leading to different physicochemical properties compared to undoped TiO_2 nanoparticles.

One of the problems in the synthesis of mesoporous TiO_2 is to achieve an appropriate balance between the hydrolysis and condensation processes of the titanium precursor. A slow hydrolytic condensation could lead to a small surface area in pure mesoporous TiO_2, because small quantities of water influence the reactivity of titanium precursor materials, and affects polymerization of TiO_2 [25]. On the other hand, higher reactivity of the titanium precursor towards hydrolysis and condensation leads to denser inorganic networks, which is promoted by the influence of hydrated RE precursors. In that way, relatively higher surface area and pore diameter are expected in RE-doped TiO_2 nanoparticles compared to undoped TiO_2 [25]. In sol-gel synthesis of anatase, TiO_2 nanoparticles crystallize with a pore diameter in the range of 3.26–6.4 nm and the surface area in the range of 25–117 m^2/g [13, 18, 22–28, 38]. In the low-concentration RE-doped anatase TiO_2 nanoparticles annealed at the intermediate temperatures, pores have almost the same size as in the undoped ones. However, relatively high doping concentrations of RE ions (up to 10%) induce significant change in pore size distribution, indicating the significant process of filling the pores, additionally promoted at higher

http://dx.doi.org/10.5772/intechopen.68882

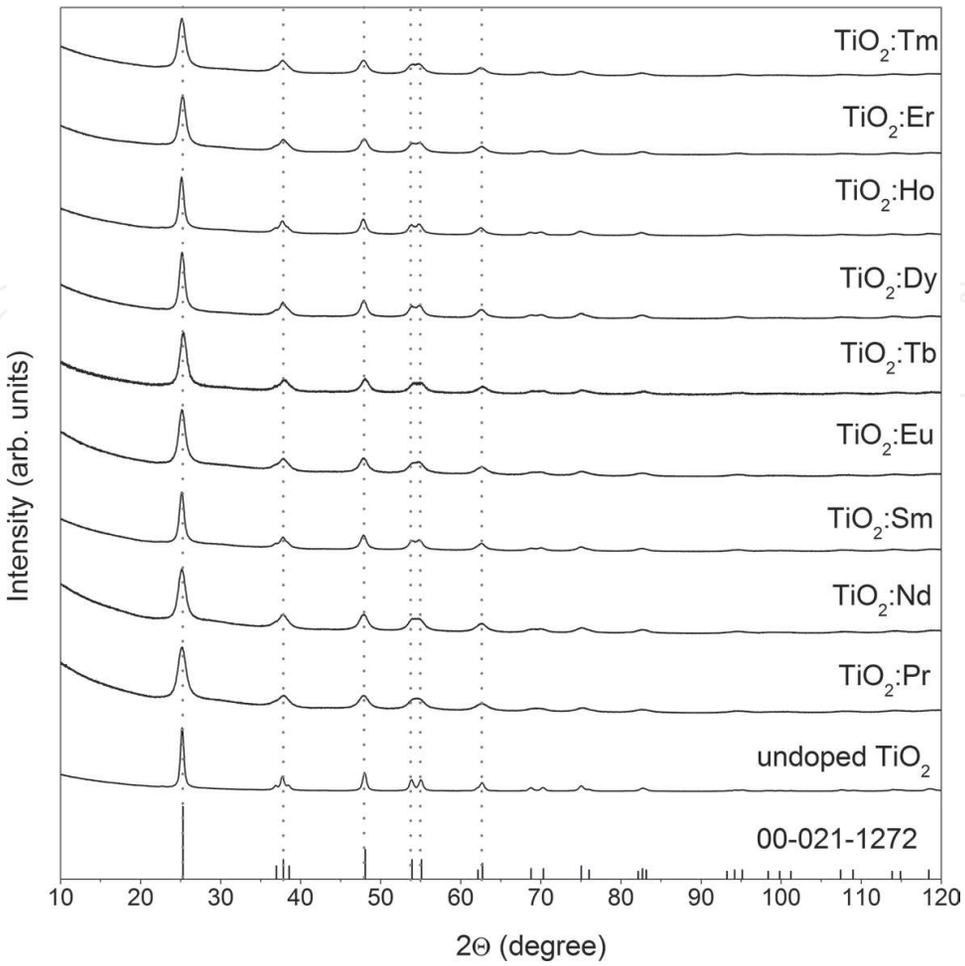

Figure 4. XRD patterns of undoped TiO_2 and TiO_2 doped with series of RE ions (RE = Pr, Nd, Sm, Eu, Dy, Tb, Ho, Er and Tm).

Sample	Crystallite size (Å)	Strain (%)	Lattice parameters $a = b$ (Å)	Lattice parameter c (Å)	Unit cell volume (Å^3)	Specific area (m^2/g)
Undoped TiO_2	149.6	0.35	3.785	9.502	136.128	9.7
TiO_2: Pr	72.1	0.85	3.803	9.508	137.512	54.4
TiO_2: Nd	68.4	0.46	3.796	9.505	136.963	101.5
TiO_2: Sm	103.1	0.48	3.804	9.521	137.643	68.2
TiO_2: Eu	81.6	0.73	3.796	9.494	136.805	52.4
TiO_2: Dy	101.3	0.56	3.794	9.505	136.189	87.4
TiO_2: Tb	83.1	0.66	3.789	9.494	136.301	–
TiO_2: Ho	102.63	0.40	3.806	9.535	138.120	81.0
TiO_2: Er	81.3	0.68	3.797	9.516	137.194	68.2
TiO_2: Tm	79.5	0.58	3.801	9.528	137.657	63.7

Table 5. XRD and BET results of undoped TiO_2 and RE doped TiO_2.

temperatures. For most of the RE ion-doped anatase TiO_2 nanoparticles, porosity can be presented by unimodal distributions, while the bimodal distribution may occur in some cases of higher doping concentration of RE ions and higher calcination treatments, when their pore diameter exceeded 100 nm [38].

The adsorption isotherms of RE-doped TiO_2 nanoparticles prepared by sol-gel route show type IV behaviour with the typical hysteresis loop. Undoped TiO_2 often show tails in their hysteresis loops at higher relative pressure, which are usually attributed to wide distribution of mesopores with some percentage of macropores (>50 nm). With the increase in calcination temperature, the crystallite size increases, also resulting in the significantly larger average pore size, but also with reduction in surface area values. The RE-doped TiO_2 are characterized by high degree of pore-size uniformity and a well-defined narrow pore size distribution without any contribution of macropores. On the contrary to the undoped TiO_2, high surface area can be retained even at relatively high temperatures [22]. Different trends are observed in samples prepared by impregnation sol-gel synthesis based on the later addition of RE metals that can lead to blockage pores and the formation of agglomerations due to low dispersion over the surface. The comparison of surface areas reveals that the specific surface area decreases by adding the metal oxides on the surface [71, 74]. The pore diameter of the RE-doped TiO_2 nanoparticles prepared with co-precipitation synthesis is larger and basically consists of some percentage of macropores (>50 nm). The formation of macroporous structure in the RE-doped TiO_2 nanoparticles was attributed to the agglomerations of TiO_2 particles and higher calcination treatment, as already known that higher calcination temperature will facilitate the growth of grains, obviously the smaller pores endured much greater stress and collapsed first during the calcination treatment [32].

RE-doped TiO_2 prepared by hydrothermal route shows higher Brunauer, Emmett and Teller (BET) surface area values when compared to undoped TiO_2. Probably, the increase in the BET surface area with increasing the doping level of RE ions is a consequence of smaller crystallite size for RE-doped TiO_2 [28]. However, the lack of linear correlation between the crystallite size of TiO_2 and the specific surface area may suggest that small amounts of RE_2O_3 were accumulated on the surface of TiO_2 nanoparticles resulting in higher surface area [28].

The specific surface area of the synthesized materials estimated by BET method is summarized in **Table 5**. The significant influence of RE^{3+} ions in doped anatase TiO_2 is obvious by the huge increase in the surface area of doped materials compared to the undoped one. The crystallite size and BET surface area have no linear correlation, suggesting a small amount of RE_2O_3 accumulated on the surface of TiO_2. The result could also be discussed regarding agglomeration of nanoparticle which is unavoidable in this kind of synthesis.

Transmission electron microscopy (TEM) was performed in order to investigate the surface morphology of the undoped TiO_2 nanopowder and nanopowders doped with the series of RE ions. RE-doped TiO_2 nanopowders were prepared by the sol-gel method using the series of RE (Pr, Nd, Sm, Eu, Dy, Tb, Ho, Er and Tm) oxides and titanium(IV)-isopropoxide, as previously discussed. The final calcination treatment is carried out at a temperature of 420°C for 2 h. As it can be seen from **Figure 5(A)**, the undoped sol-gel anatase sample consists of densely aggregated crystalline nanoparticles of irregular shapes, and variable dimensions of about 10–20 nm in size. Using selected area electron diffraction (SAED) technique, local crystal structure was confirmed to be pure anatase phase. The ring pattern was indexed by ICDD card no. 00-021-1272 with rings that correspond to 101, 004, 200, 105, 211 and 204 main reflections,

presented in **Figure 5(B)**. The presence of rings suggests polycrystalline sample, and the characteristic grainy appearance of the rings suggests that crystallites have a size of 20 nm or more, suggesting only few joint unit cells per particle.

In **Figure 6**(**A–I**), TEM of RE-doped TiO_2 nanopowders is collected at different magnifications, all showing a bar of 20 nm. All of the doped samples show agglomerated nanoparticles, only the estimated particles are smaller in size compared to the undoped sample.

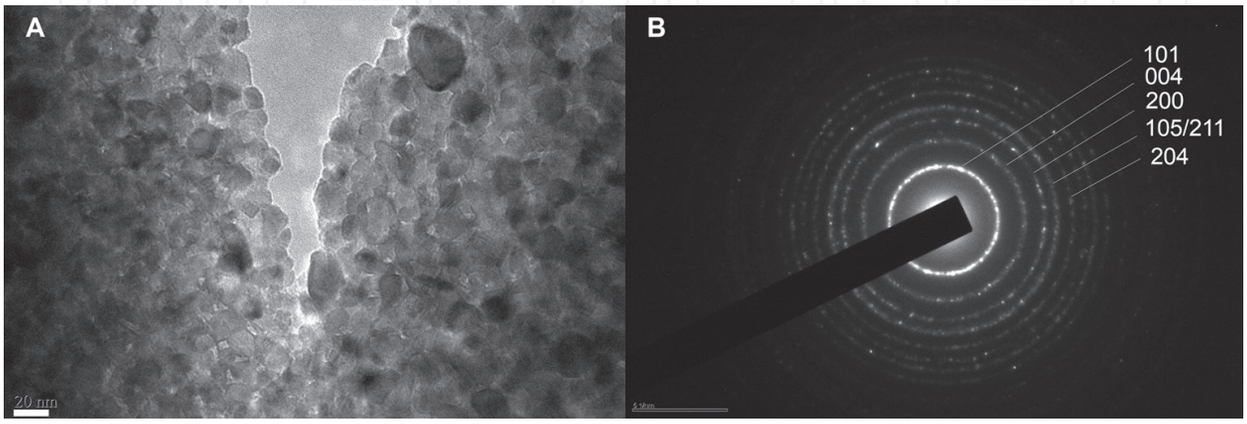

Figure 5. Transmission electron micrograph of undoped TiO_2 nanopowders recorded at magnification of ×67,000 (A), with corresponding selected area electron diffraction (B).

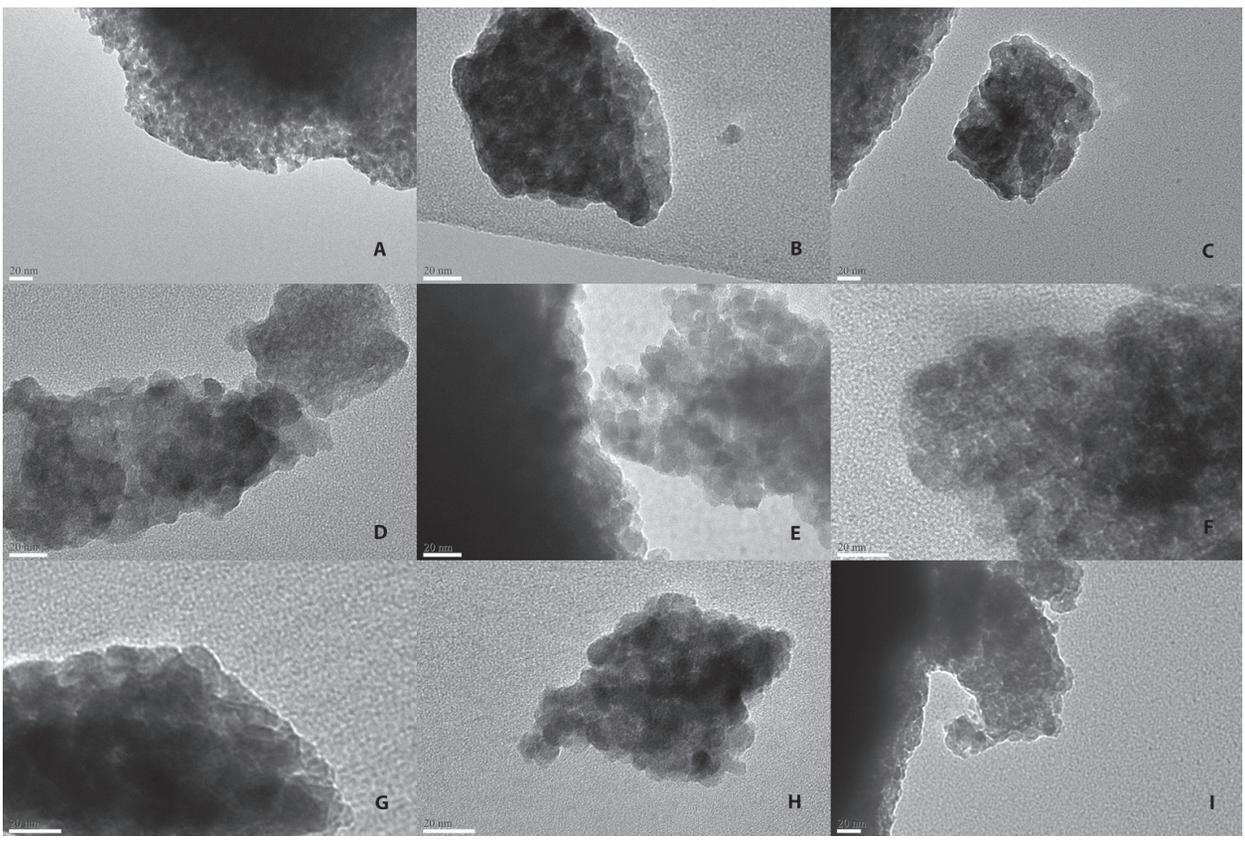

Figure 6. Transmission electron micrographs of RE-doped TiO_2 nanopowders at different magnification with bar of 20 nm: (A) TiO_2:Pr, (B) TiO_2:Nd, (C) TiO_2:Sm, (D) TiO_2:Eu, (E) TiO_2:Dy, (F) TiO_2:Tb, (G) TiO_2:Ho, (H) TiO_2:Er and (I) TiO_2:Tm.

4. The influence of rare earth doping on photocatalytic activity of anatase TiO_2 nanoparticles

One of the main challenges in photocatalytic research is the increase of spectral sensitivity of TiO_2 from ultraviolet (UV) to visible (VIS) spectrum. Incorporation of various RE ions into the anatase TiO_2 can increase the photocatalytic activity by enhancing the light absorption, adjustment of the phase structure, crystallinity, doping concentration, surface area and morphology. An overview of literature where RE-doped TiO_2 was used as a photocatalyst in respect to variables to experiments is given in **Table 6**. For detailed information about the type of artificial light source, time of illumination, as well as the percentage of dye degradation, the readers are advised to inquire the reference list provided in **Table 6**.

Dopant ion	Optimal doping conc. (%)	Synthesis method	Optimal calcination temperature (°C)	Crystalline phase	Dye	Refs.
Sc	2	Sol-gel	500	A + B	Rhodamine B	[37]
Y	1.5	Sol-gel	500	A	Methyl orange	[31]
Y	–	Hydrothermal	150	A	Methyl orange	[47]
Y	0.25	Hydrothermal	400	A	Phenol	[28]
Y	0.3	Hydrothermal	400	A + R	Phenol	[51]
La	0.3	Hydrothermal	400	A + R	Phenol	[51]
La	1	Sol-gel	550	A	Direct blue dye (DB53)	[75]
Pr	0.3	Sol-gel	450	A	Herbicide metazachlor	[33]
Pr	0.25, 0.5	Hydrothermal	400	A	Methyl orange	[55]
Pr	0.3	Hydrothermal	400	A + R	Phenol	[51]
Nd	0.3	Hydrothermal	400	A + R	Phenol	[51]
Nd	1	Sol-gel	550	A	Direct blue dye (DB53)	[75]
Sm	0.3	Sol-gel	500	A	Diuron	[38]
Sm	0.7	Sol-gel	500	A	Remazol red RB-133	[29]
Sm	1	Sol-gel	500	A	Methylene blue	[42]
Sm	1	Sol-gel	550	A	Direct blue dye (DB53)	[75]
Eu	0.5–2.0	Sol-gel	400	A	Methylene blue	[39]
Eu	1	Sol-gel	500	A	Rhodamine B	[71]
Eu	1	Sol-gel	420	A	Crystal violet	[27]

Dopant ion	Optimal doping conc. (%)	Synthesis method	Optimal calcination temperature (°C)	Crystalline phase	Dye	Refs.
Eu	1.3	Sol-gel	500	A	Remazol red RB-133	[29]
Eu	1	Sol-gel	550	A	Direct blue dye (DB53)	[75]
Eu	1.5	Sol-gel	500	A	Methylene blue	[30]
Eu	0.5	Hydrothermal	50	A	Phenol	[56]
Gd	1	Sol-gel	550	A	Direct blue dye (DB53)	[75]
Gd	5	Sol-gel	800	A + $Gd_2Ti_2O_7$	Methylene blue	[22]
Gd	0.3-0.6	Magnetron sputtering	1000	R	Methyl orange	[65]
Tb	0.7	Sol-gel	500	A	Remazol red RB-133	[29]
Ho	0.3	Sol-gel	500	A	Methyl orange	[23]
Ho	0.5	Sol-gel	600	A	Methyl orange	[23]
Ho	0.5	Sol-gel	500	A	Methyl orange	[36]
Ho	0.75	Hydrothermal	150	A + R	Methylene blue	[46]
Er	1.5	Sol-gel	500	A	Orange I	[26]
Er	2	Hydrothermal	400	A	Phenol	[48, 49]
Er	0.5	Electrospinning	500	A	Methylene blue	[61]
Yb	1	Sol-gel	550	A	Direct blue dye (DB53)	[75]

Table 6. RE-doped TiO_2 used as photocatalyst in recent photocatalytic studies.

Initially, when TiO_2 is exposed to light, it produces two types of charge carriers: electrons (e^-) in conduction band and holes (h^+) in valence band, as presented in **Figure 7(a)**. These e^-/h^+ pair generations follow the processes of charge separation and migration to the surface. At the surface, active species in valence band (h^+_{vb}) reacts with adsorbed water producing $OH^\bullet$ radical and proton (H^+). At the same time, active species in conducting band (e^-_{cb}) reacts with oxygen to produce active $O_2^{\bullet-}$ radical. The radical reacts with the proton and produces $OH_2^\bullet$ radical. When paired, the $OH_2^\bullet$ radicals produce H_2O_2 which degrades into two $OH^\bullet$ radicals. The formation of $OH^\bullet$ is crucial for the degradation of organic dye. However, the rate of recombination of photogenerated e^-/h^+ pairs is very fast (few nanoseconds) and substantial number can be recombined with just the release of heat [76]. When RE-doped TiO_2 is used as photocatalyst, incorporation of RE ions into the TiO_2 host creates charge imbalance. With increasing charge imbalance, more hydroxide ions are being adsorbed on the TiO_2 surface. Hydroxide ions (OH^-) restrain the recombination of e^- and h^+, and additionally react with holes to produce surface

hydroxyl radical (OH•), which substantially improve the photocatalytic degradation of dye [26, 28]. The main disadvantage in the application of anatase TiO_2 as catalyst is dominant absorption in UV caused by its band gap (E_g ~3.2 eV). One approach to enhance absorption in VIS is doping. In the means of energy, doping can alter absorption threshold to lower energies. Incorporation of RE ions into the TiO_2 host modifies the band gap of TiO_2 with sub-band-gap energy levels of RE ions, as illustrated in **Figure 7(b)** [64, 77]. These energy levels offer electronic transition from the TiO_2 valence band to the empty RE ion sub-band-gap energy levels. These transitions require less energy than TiO_2 valence-to-conduction band transition and can be induced by visible light. In that way, RE ions in the TiO_2 host enhance the separation of e^- and h^+, contributing to photocatalytic degradation of organic dyes [28].

The main focus on the photocatalytic activity of RE ions incorporated into the anatase TiO_2 is the influence of RE-doping concentration [23, 26, 28, 31, 46, 56, 61, 65]. On the other hand, reports of comprehensive investigation of the type of RE ions in TiO_2 matrix, in order to predict the influence of dopants on the photocatalytic activity under UV and visible light, are scarce [51, 75, 78]. The results for photocatalytic activity of 1 at.% RE (RE = Pr, Nd, Sm, Eu, Dy, Tb, Ho, Er and Tm)-doped anatase TiO_2 nanopowders are presented in **Figure 8**. All of doped nanopowders were prepared in the same way, as presented in **Figure 3**. Methylene orange (MO) aqueous solution with a concentration of 5 mg/l was used in all experiments. Solutions were photocatalytically treated up to 4 h with 0.1 g of undoped- and RE-doped TiO_2 nanopowders. UV-VIS light irradiation Ultra-Vitalux 300 W, Osram lamp was used in all experiments in order to simulate the solar radiation. Absorptions of MO solution aliquots were measured after 0, 5, 10, 20, 30, 60, 90, 180 and 240 min of illumination. The results of photodegradation of MO, observed at a maximum absorbance of MO at 464 nm, for Ho-doped TiO_2 nanopowder, are presented in **Figure 8(a)**. The results of MO degradation for all samples were calculated by $Degradation\ (\%) = \left[\frac{(C_0 - C)}{C_0}\right] \times 100\%$, where C_0 is the initial concentration of MO solution and C is the concentration of MO solution after 4 h, and is given in **Figure 8(b)**. These results show that the incorporation of the RE ions into the TiO_2

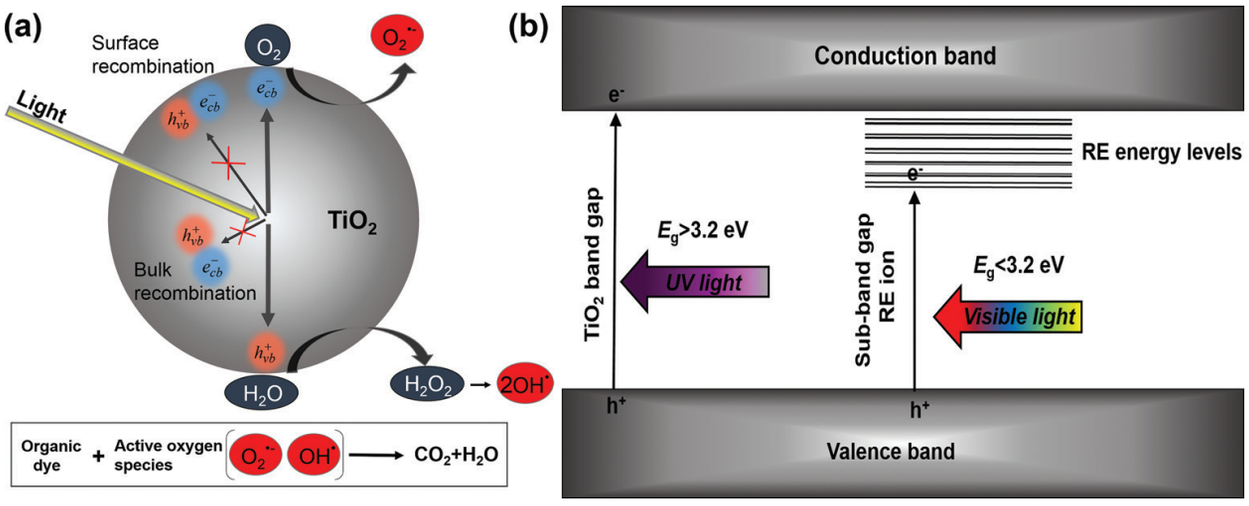

Figure 7. (a) Basic photocatalytic mechanism under UV or visible light irradiation. (b) Modification of band gap with sub-band-gap energy levels of RE ions.

matrix may bring a positive effect on the photocatalytic activity of TiO_2, as presented in **Figure 8(b)**. The reasons could be attributed to the synergetic effects of anatase phase stability, reduced crystallite size, relatively large surface area, significant improvement of the separation rate of photogenerated e^-/h^+ pairs and efficient absorption of visible light due to sub-energy levels of RE ions into the band gap of TiO_2.

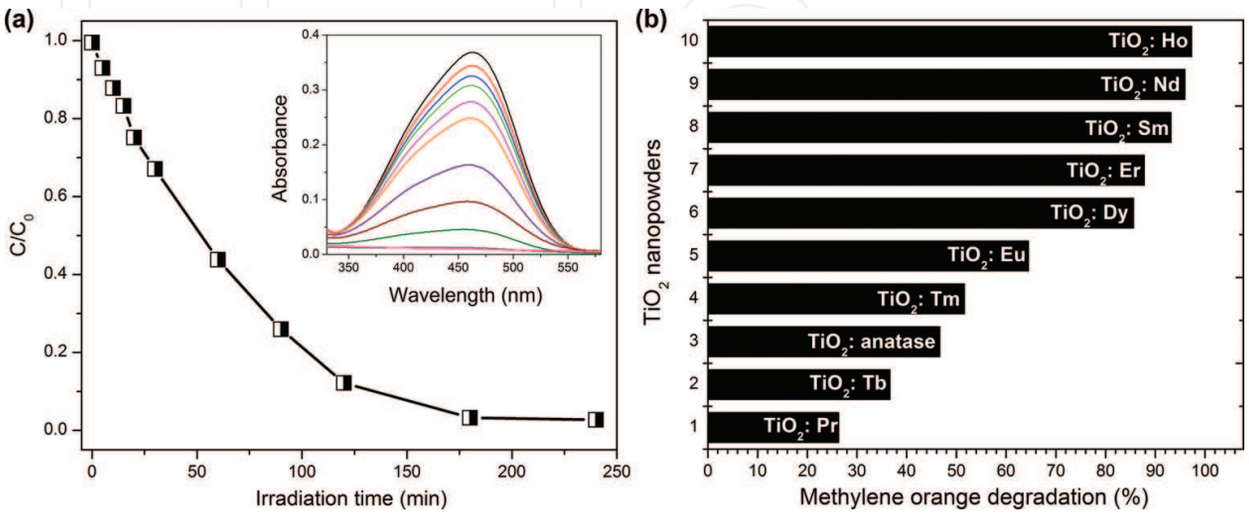

Figure 8. (a) The concentration of MO solution as a function of irradiation time for Ho-doped TiO_2 used as photocatalyst, inset: the absorption spectra of MO after different illumination times. (b) Photocatalytic degradation of MO after 4 h for various RE-doped TiO_2, with the fixed concentration of RE ions.

5. Optical properties of rare earth-doped anatase

When light interacts with matter, the material can absorb, transmit or reflect some part of the light. Absorption spectroscopy is a method to measure absorption as a function of wavelength or frequency. Since light cannot penetrate opaque samples such as powders and other solids, it is reflected on the surface of the samples. Spectrometers with integrating spheres measure the change of reflected light of a surface and compare it to a standard, most often barium sulphate, which is taken to be 100% of reflected light. Then, the obtained value is relative reflectance, and the reflectance spectrum provides the information of interaction of light in the sample as a function of wavelength. In that manner, reflectance can be directly correlated with absorption. Nowadays, research-grade spectrophotometers can combine detectors and extend detected light up to the near-infrared region of 1400 nm.

Some of the absorbed light can subsequently be emitted as light, as was already discussed in Section 1. Then, the radiative processes can be observed by photoluminescence spectroscopy (PL). In steady-state PL spectroscopy, we primarily refer to excitation and emission spectroscopy measurements obtained by a continual light source which emits a constant number of photons in time. Since exciting of electrons takes about 10–15 s^{-1}, following energy dissipation, whether radiative of non-radiative, is a much slower process so the number of excited electrons could be considered as constant. Absorption spectroscopy could suggest the wavelength

that could be used to gain luminescence, but not all absorption result in emission. When we refer to the Jablonski diagram, it is obvious that absorption can occur to several excited singlet states, such as S_1, S_2, and so on, and expected emission normally occurs only from the lowest excited singlet or triplet states, S_1 and T_1. In excitation spectrum, a single emission detection wavelength is chosen that corresponds to an expected band in the emission spectrum. The excitation source is then scanned through wavelength region, and the intensity of the emission at the single selected wavelength is scanned in a function of excitation wavelength. The output of absorption and excitation spectrum is not the same, although detected maxima (or minima) at the same wavelength suggest the same excited energy levels. In luminescence emission spectroscopy, a wavelength of exciting light is selected, and emission spectrum is obtained by detecting the intensity of the emitted light as a function of wavelength. In downconversion emission spectroscopy, emitted luminescence is recorded in the spectral range above the excitation wavelength to longer wavelengths, up to the region where luminescence is expected. It was then of interest to study the influence of rare earth doping on anatase nanoparticles by the interpretation of absorption (reflectance), excitation and emission spectroscopy methods.

Samples of RE-doped anatase materials are in literature most often characterized by a positioning of the threshold of absorption of doped samples and compared to the undoped ones. Even with the reduction of nanoparticles size after rare earth ions incorporation, the difference in extrapolated slopes after Kubelka–Munk transformations in doped and undoped nanopowder samples should not be ascribed to quantum confinement effect, since particle sizes exceed the Bohr radius several times [18, 79]. Some modifications of materials density of states after the incorporation of trivalent rare earth ions are the most probable reason for small differences in observed band gaps, which is highly dependent on the synthesis procedure and the RE dopant. Kubelka-Munk transformation of reflectance spectra of RE^{3+}-doped anatase TiO_2 measured over the 360–440 nm spectral range is presented in **Figure 9**.

5.1. Praseodymium

The absorption of praseodymium ion in TiO_2 hosts is reported in Refs. [28, 55, 80, 81]. From reflectance spectrum of TiO_2:Pr presented in **Figure 10(a)**, absorptions of Pr^{3+} ions in TiO_2 absorption edge are observed at approximately 445, 480 and 595 nm that could be attributed to the transition from $^3H_4$ ground state to the $^3P_{2\text{-}0}$ and $^1D_2$ excited states of the Pr^{3+} ions. Low wide absorption at around 1000 nm could be assigned to $^1G_4$ excited state. Excitation spectrum is recorded at a fixed emission wavelength of 493 nm in the range of 260–460 nm, presented in **Figure 10(b)**. Two wide excitations are observed at 325 and 447 nm. The excitation of 447 nm was used to obtain emission spectrum in the range of 475–780 nm. Even though the room temperature emission maxima are wide, several transitions can be assigned as follows: $^3P_0 \rightarrow {}^3H_5$ (493 and 536 nm), $^3P_0 \rightarrow {}^3H_6$ (620 nm) and $^3P_0 \rightarrow {}^3F_2$ (650 nm), as can be seen in **Figure 10(c)**. $^1D_2$–$^3H_4$ transition is not observed, suggesting high concentration of Pr^{3+} ions in TiO_2 matrix, where cross-relaxation between neighbouring Pr^{3+} ions occurs [82].

5.2. Neodymium

The absorption of neodymium ion in TiO_2 hosts is reported in a spectral range up to 700 nm [41] and up to 1200 nm [34, 83]. From reflectance spectrum of TiO_2:Nd presented in

http://dx.doi.org/10.5772/intechopen.68882

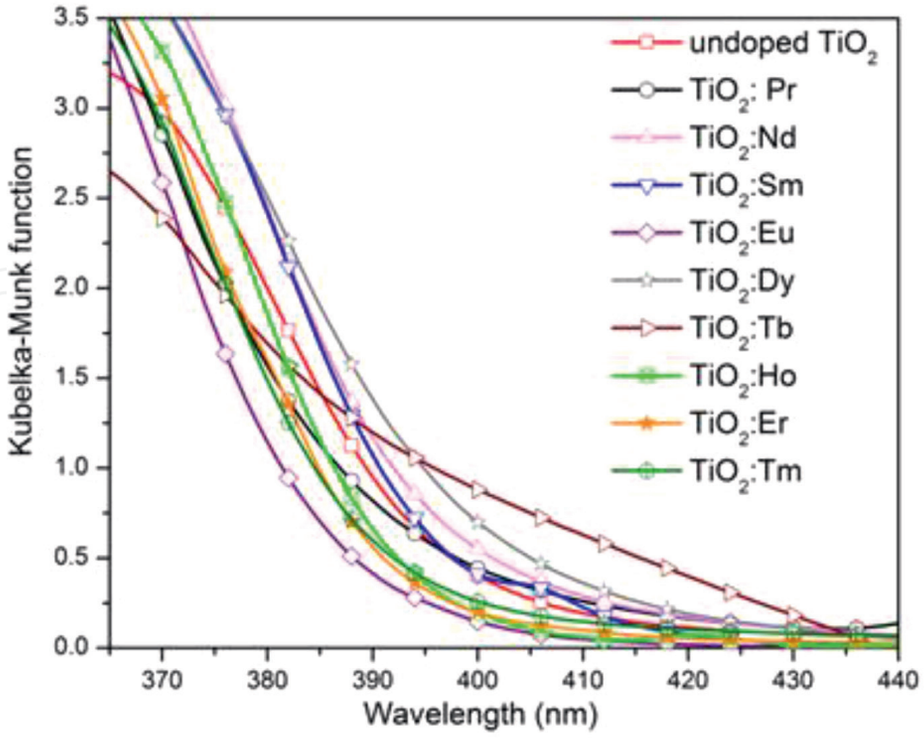

Figure 9. Kubelka-Munk transformation of reflectance spectra of RE^{3+}-doped anatase TiO_2 measured over the 360–440 nm spectral range.

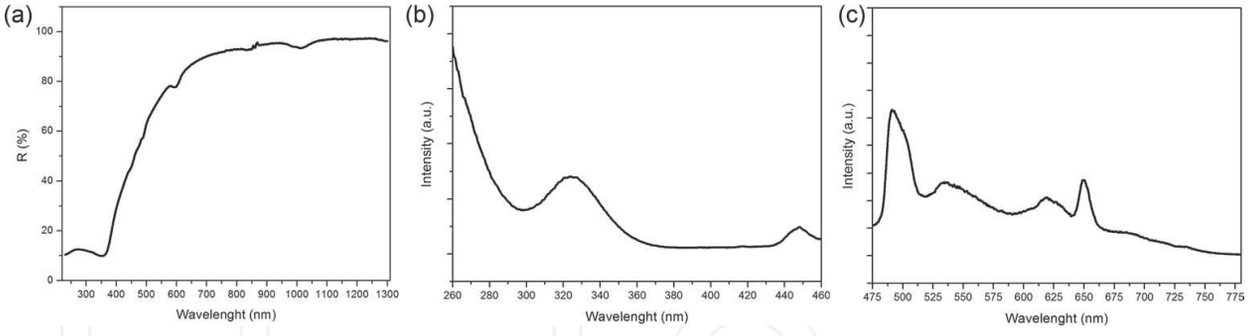

Figure 10. (a) Reflectance, (b) excitation and (c) emission spectra of anatase TiO_2:Pr nanopowders.

Figure 11(a), eight absorptions from ground $^4I_{9/2}$ to excited energy levels of Nd^{3+} ions in TiO_2 are observed and assigned in energy-level diagram in **Figure 11(b)**. Intense emission of Nd^{3+} can be obtained in the IR spectral range above 850 nm, **Figure 11(c)**. Three transitions from $^4F_{3/2}$ to its lower $^4I_{9/2}$, $^4I_{11/2}$ and $^4I_{13/2}$ are obtained with an excitation of 752 nm. The transitions correspond well with the reported data of Nd^{3+} in anatase matrix [34, 40, 84]. The position and shape of $^4F_{3/2} \rightarrow {}^4I_{9/2}$ strongly suggest Nd-doped TiO_2 anatase sample, without the presence of other compositions of segregated neodymium oxide and neodymium titanate phases [34].

5.3. Samarium

In reflectance measurements presented in **Figure 12(a)**, significant absorptions of Sm^{3+} ion can be observed, with maxima positioned at around 480 nm, which corresponds to absorption

into $^4G_{5/2}$, and several strong absorptions positioned at around 947, 1080 and 1230 nm. Room temperature excitation spectrum is in the range of 310–550 nm at a fixed emission at 585 nm shown in **Figure 12(b)**. Strong wide band below 400 nm, with maximum at about 365 nm, is characteristic for Sm^{3+} in TiO_2 matrix that is assigned to charge transfer from the oxygen ligands in TiO_2 to Sm^{3+} ion [18, 29, 34, 35]. Several smaller and combined excitations at around 411 and 476 nm could be assigned to $^6G_{7/2}$ or $^6P_{5/2}$ and $^4I_{13/2,}$ respectively [18, 34]. In **Figure 12(c)**, room temperature emission spectrum in the range of 400–700 nm obtained after excitation into charge transfer at 365 nm showed only characteristic emissions from $^4G_{5/2}\rightarrow{}^6H_{5,7,9/2}$ energy levels. It is worth mentioning that the same spectral features are obtained also with exciting directly into Sm^{3+} ion by excitation with 411 nm, with all the intensities decreased as expected from the excitation spectrum. No complete splitting of Stark components caused by ligand field that are obvious at room temperatures and are in correspondence with the literature is attributed to the large number of defect at the surface [18, 29, 34, 35, 42]. When directly excited, the enhancement of Sm^{3+} emission in TiO_2 by codoping with silver dopant, caused by combined influence of plasmonic effects and sensitizing of Sm^{3+} emission by silver ions, is reported in TiO_2 films [85].

5.4. Europium

The lowest excited level ($^5D_0$) of Eu^{3+} ion is a non-degenerate ($J = 0$) singlet level, along with crystal field non-sensitive $^5D_0\rightarrow{}^7F_1$ transition and hypersensitive $^5D_0\rightarrow{}^7F_2$ emissions simplify the interpretation of emission spectra. Consequently, europium ion incorporated in

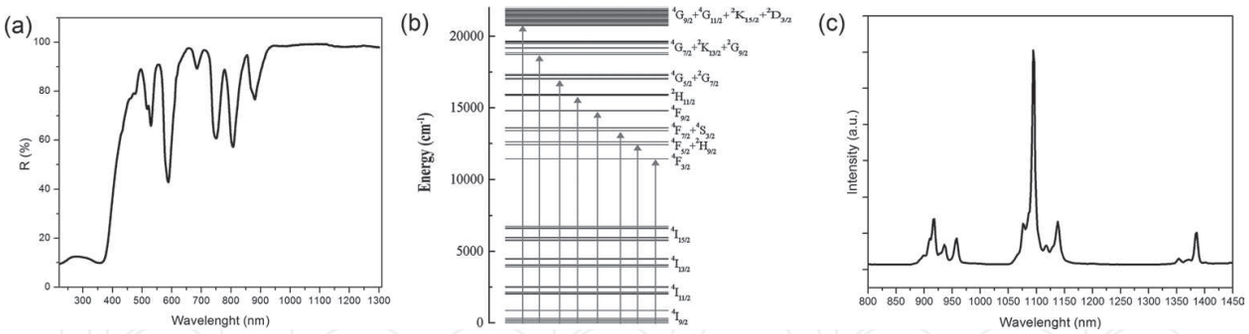

Figure 11. (a) Reflectance, (b) energy-level diagram and (c) emission spectra of anatase TiO_2:Nd nanopowders.

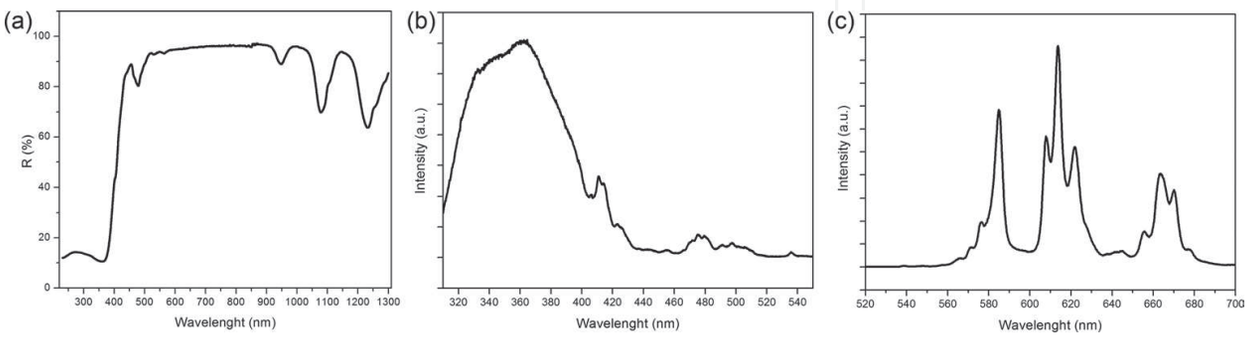

Figure 12. (a) Reflectance, (b) excitation and (c) emission spectra of anatase TiO_2:Sm nanopowders.

various matrices is often used as a luminescent probe ion in photoluminescence spectroscopy [86–90]. In **Figure 13(a)**, after a sharp rise of absorption in UV spectral range below 400 nm, low-intensity Eu^{3+} absorptions from $^7F_0 \rightarrow ^5D_2$ at around 465 nm and $^7F_0 \rightarrow {}^5D_1$ at around 535 nm transitions are clearly observed. Those transitions are also present in excitation spectrum (**Figure 13(b)**) obtained with an emission fixed at 613 nm. Four dominant excitation bands originate from direct excitation of Eu^{3+} ions from ground $^7F_0$ level to $^5L_6$ (394 nm), $^5D_3$ (414 nm), $^5D_2$ (464 nm) and $^5D_1$ (532 nm) levels. By excitation into $^5L_6$ level, room temperature emission spectrum presented in **Figure 13(c)** clearly shows that emissions from $^5D_0 \rightarrow {}^7F_J$ (J = 0–4) transitions are centred at around 580, 593, 613, 653 and 702 nm, respectively. A small emission observed at 540 nm is emission from higher excited $^5D_1$ level. The positions and relative intensities of wide emissions are in correspondence with extensive literature data [18, 29, 42, 45, 52, 53, 63, 67, 69, 91]. In some presented results of low-temperature site-selective spectroscopy of the materials, three possible positions of Eu ion in TiO_2 can be distinguished: Eu^{3+} can occupy Ti^{4+} site, it could enter into the interstitial site in the chain structure, or a third possible site for dopant cation is low-symmetry-distorted sites near nanoparticle's surface [18, 19, 91].

5.5. Terbium

Terbium ions often show a tendency to be stabilized by matrices in two valence states, +3 and +4. Only lower valence state is optically active in visible spectrum. The mixture of valences can additionally disturb crystallinity of matrices and introduce additional vacancies, and hence perturbations in energy states. In absorption spectra presented in **Figure 14(a)**, no clear absorption of Tb^{3+} ion can be resolved, but significant difference in absorption threshold of TiO_2 is obvious, suggesting possible weak absorption of energy in the range below 500 nm. Some reports state no or very weak emission of Tb^{3+} ion in TiO_2 matrix attributed to the mismatch of the energy levels of the $^5D_4$-emitting state of Tb^{3+} with band gap of TiO_2 [18, 29, 60, 69]. Nevertheless, as presented in **Figure 14(b, c)**, excitation and emission spectra are actually obtained. At an emission wavelength of 545 nm, excitation spectrum was measured in the range of 300–500 nm. Wide charge transfer band can be seen below 350 nm, and excitations of Tb^{3+} ion from $^7F_6$ ground level to $^5D_4$ excited level are observed at 484 nm, two excitations to $^5D_2$ 368 nm and $^5D_3$ at 377 nm. When excited into $^5D_4$ excited energy level with 484 nm, emission spectrum in the range of 510–780 nm

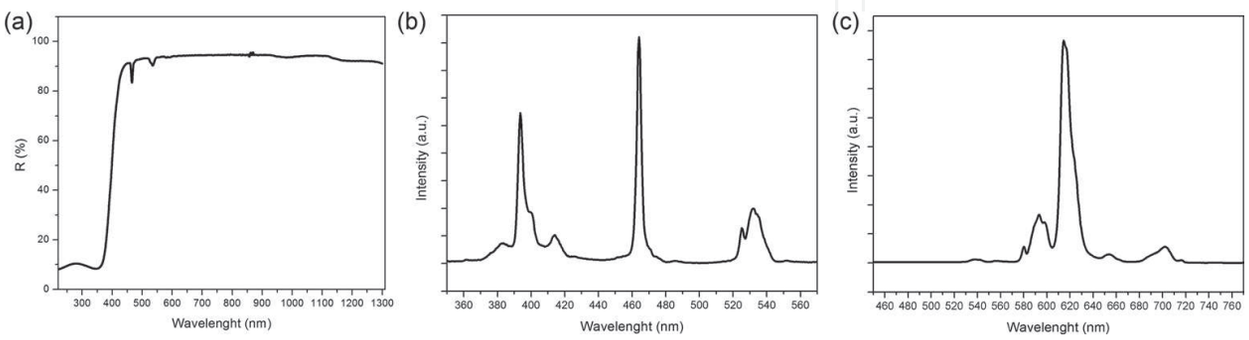

Figure 13. (a) Reflectance, (b) excitation and (c) emission spectra of anatase TiO_2:Eu nanopowders.

shows emission from $^5D_4$ to $^7F_5$ at 546 nm, $^5D_4$ to $^7F_4$ at 585 nm and $^5D_4$ to $^7F_3$ at 622 nm. The green emission at 546 nm is the dominant one. The findings are in good agreement with the literature [29, 60, 64, 69].

5.6. Dysprosium

Reflectance spectrum of Dy^{3+} ions into TiO_2 presented in **Figure 15(a)** shows low-wavelength bands of Dy^{3+} that overlaps with the absorption threshold of anatase at 450 and 470 nm and intense longer wavelength bands in the range of 700–1300 nm. Excitation spectrum of TiO_2:Dy^{3+} sample recorded at room temperature in the 300–500 nm range with a fixed emission wavelength of 577 nm showed excitations corresponding to electron transitions from the Dy^{3+} ground states to the excited states: $^4K_{17/2}$ at 391 nm, $^4G_{11/2}$ at 425 nm, $^4I_{15/2}$ at 452 nm and $^4F_{9/2}$ at 472nm, **Figure 15(b)**. When excited with 425 nm, dominant luminescence is observed with two bands observed in the blue spectral region at 483 nm, which correspond to magnetic-dipole $^4F_{9/2}\rightarrow{}^6H_{15/2}$ transition and in yellow spectral region at 580 nm, which correspond to electric-dipole $^4F_{9/2}\rightarrow{}^6H_{13/2}$ transition, **Figure 15(c)**. A low-intensity emission is observed in the red region at 674 nm that corresponds to $^4F_{9/2}\rightarrow{}^6H_{11/2}$ transition. With literature proposing no luminescence from Dy^{3+} ion in anatase host [92], this finding shows that nanocrystalline anatase powders can actually host this ion that can successfully be excited and luminescence can be observed.

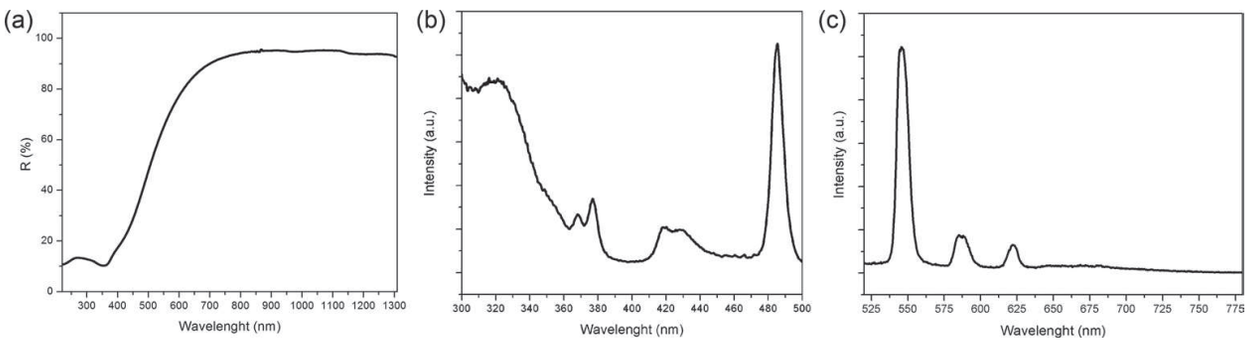

Figure 14. (a) Reflectance, (b) excitation and (c) emission spectra of anatase TiO_2:Tb nanopowders.

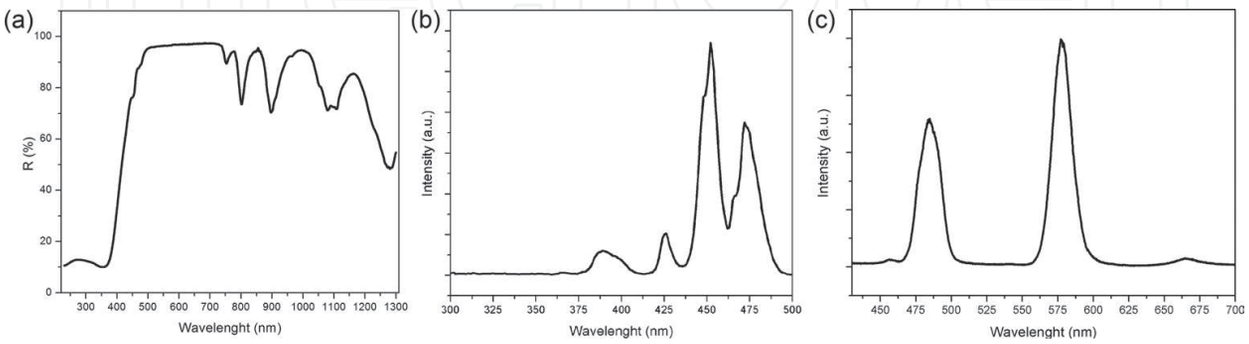

Figure 15. (a) Reflectance, (b) excitation and (c) emission spectra of anatase TiO_2:Dy nanopowders.

5.7. Holmium

Among all RE^{3+} ions doped in nanocrystalline anatase TiO_2 powders in this work, Ho^{3+} has the most pronounced absorptions in VIS. As can be seen from **Figure 16(a)**, intense bands can be observed at 420, 456, 490, 542 and 645 nm and smaller intensity bands are observed at 890, 1150 and 1200 nm. In excitation spectrum at fixed emission wavelength of 554 nm presented in **Figure 16(b)**, several excitations centred at around 422, 452, 468 and 493 nm show several possible energies for potential emission. As can be seen in **Figure 16(c)**, when excited with 452 nm, emission spectra in the range of 500–700 nm show dominant emissions from $^5F_4/^5S_2 \rightarrow {}^5I_8$ transitions at about 545, 554, and 559 nm, and emission from $^5F_5 \rightarrow {}^5I_8$ transition with maximum centred at 665 nm. Emissions from the same transitions can also be observed in samples sensitized with Yb^{3+} ions, when excitation wavelength was 980 nm that corresponds to the absorption of Yb^{3+} ions, and the mechanism of obtaining luminescence is upconversion [50].

5.8. Erbium

Absorptions of Er^{3+} ions in TiO_2 matrices are reported in spectral range from UV up to 700 nm [26, 28], up to 800 nm [49], and when sensitized with Yb^{3+} ions up to 1200 nm [48]. All of the reported data correspond well with results presented in **Figure 17(a)**. Absorptions located at 452, 477, 491, 525, 655, 795 and 980 nm correspond to the transitions from $^4I_{15/2}$ to $^4F_{3/2}$, $^4F_{5/2}$, $^4F_{7/2}$, $^2H_{11/2}$ and $^4S_{3/2}$, $^4F_{9/2}$, $^4G_{9/2}$, $^4I_{11/2}$, respectively. In excitation spectrum shown in **Figure 17(b)**, with fixed emission of 565 nm, some low-intensity excitations can be noticed at around 378, 410 and 453 nm. More pronounced excitations can be observed at 488 and 525 nm. In order to characterize emissions in the range of 520–700 nm, excitation wavelength of 488 nm was used, and the spectrum is presented in **Figure 17(c)**. From the combination of $^2H_{11/2} \rightarrow {}^4I_{15/2}$ and $^4S_{3/2} \rightarrow {}^4I_{15/2}$ transitions, wide emissions can be observed in the range of 540–575 nm, as also reported in Refs. [42, 92].

5.9. Thulium

Absorption of thulium ion in the sample presented in **Figure 18(a)** shows small absorption at 470 nm, as well as stronger absorptions at 690, 795 and 1210 nm. Excitation spectrum with

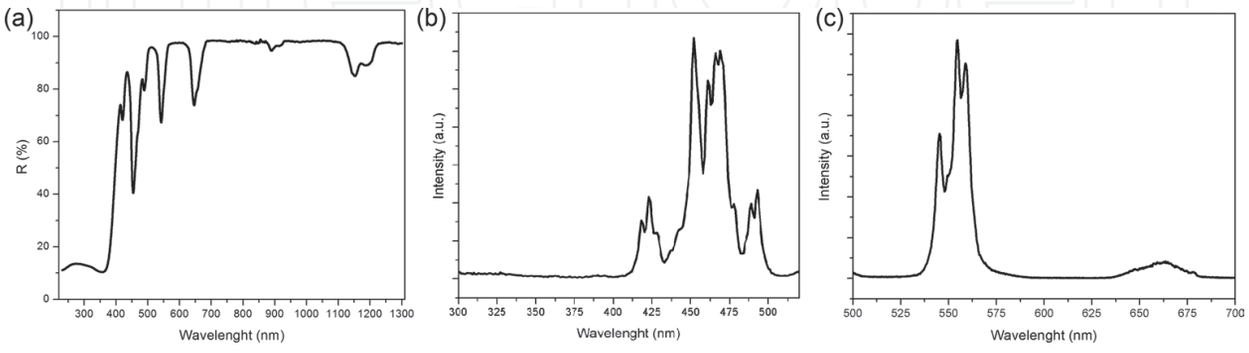

Figure 16. (a) Reflectance, (b) excitation and (c) emission spectra of anatase TiO_2:Ho nanopowders.

a fixed emission at 495 nm showed poor optical answer with some picks that most probably originate from defect, **Figure 18(b)**. In order to directly excite Tm^{3+} ion 470 nm excitation was used. Emission spectrum in the range of 490–780nm presented in **Figure 18(c)** shows shoulder of maximum at 495 nm originating from $^1G_4 \rightarrow {}^5H_6$ transition and very low intensity of group of lines in the range of 650–670 nm that could be attributed to the $^1G_4 \rightarrow {}^3F_4$ transition.

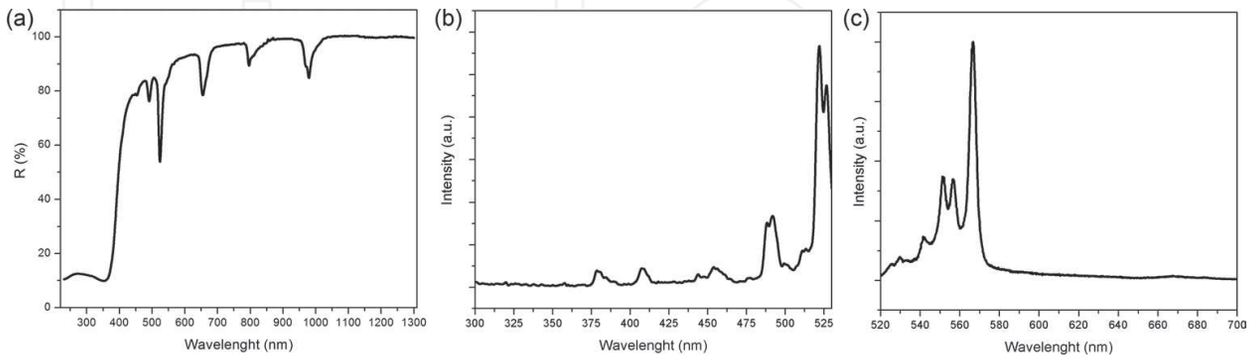

Figure 17. (a) Reflectance, (b) excitation and (c) emission spectra of anatase TiO_2:Er nanopowders.

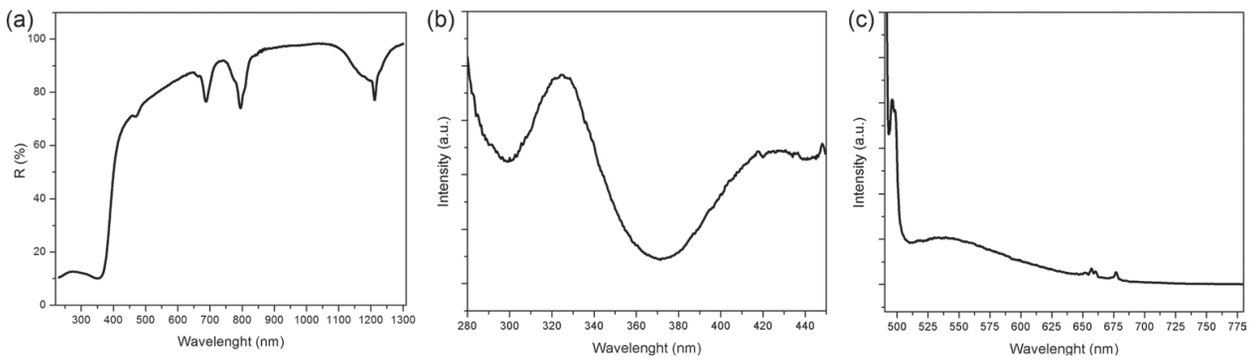

Figure 18. (a) Reflectance, (b) excitation and (c) emission spectra of anatase TiO_2:Tm nanopowders.

6. Conclusion

To conclude, the structure, morphology and optical properties of TiO_2 nanoparticles may be substantially swayed by the addition of small quantities of RE^{3+} ions. Such nanostructures deliver new options to the already broad range of important TiO_2 uses. In RE ion-doped TiO_2, anatase phase is stabilized at medium temperatures since the temperature of phase transformations shifts to higher values. The reduction of the crystallite size is readily observed and doping induces mesoporous structure with enlarged specific surface in respect to one of undoped anatase TiO_2. Thus, the photocatalytic performance of nanopowder improves with the addition of RE^{3+} in small concentrations except for Pr^{3+} and Tb^{3+}. Different rare earth ions cause TiO_2 property changes of different magnitudes. Optical properties are altered too. The modification of materials density of states after incorporation of RE^{3+} ions in TiO_2 causes changes in materials absorption which can be clearly evidenced from optical absorption

spectra. Rare earth ions may be incorporated at three different sites in TiO_2 structure: they can substitute Ti^{4+} in the bulk of particle, enter vacancy site, but they at large reside near surface in low-symmetry sites. In such cases, the characteristic RE^{3+} luminescence is observed in the case of doping with the following ions: Nd^{3+}, Sm^{3+}, Eu^{3+}, Dy^{3+}, Ho^{3+} and Er^{3+}, while luminescence of low intensity is detected for Pr^{3+}, Tb^{3+} and Tm^{3+}.

Acknowledgements

The authors thank Prof. Damien Bregiroux and Alexandre Bahezre from Université Pierre et Marie Curie—LCMCP for BET and TEM measurements. This work was done as a French-Serbian collaboration under Bilateral project no. 451-03-39/2016/09/03. The financial support for this work was provided by the Ministry of Education, Science and Technological Development of Republic of Serbia (Project 172056).

Author details

Vesna Đorđević*, Bojana Milićević and Miroslav D. Dramićanin

*Address all correspondence to: vesipka@vinca.rs

Vinča Institute of Nuclear Sciences, University of Belgrade, Belgrade, Serbia

References

[1] Shannon RD. Revised effective ionic radii and systematic studies of interatomic distances in halides and chalcogenides. Acta Crystallographica. 1976;**A32**:751-767. DOI: 10.1107/S0567739476001551

[2] Laporte O, Meggers WF. Some rules of spectral structure. Journal of the Optical Society of America. 1925;**11**(5):459-463. DOI: 10.1364/JOSA.11.000459

[3] Bünzli J-CG, Eliseeva SV. Basics of lanthanide photophysics. In: Hänninen P, Härmä H, editors. Lanthanide Luminescence: Photophysical, Analytical and Biological Aspects. Berlin Heidelberg: Springer-Verlag; 2010. pp. 1-45. DOI: 10.1007/4243_2010_3

[4] Dieke GH, Crosswhite HM. The spectra of the doubly and triply ionized rare earths. Applied Optics. 1963;**2**(7):675-686. DOI: 10.1364/AO.2.000675

[5] Dieke GH. Spectra and Energy Levels of Rare Earth Ions in Crystals. New York, NY: Interscience Publishers; 1968. 401 p.

[6] Peijzel PS, Meijerink A, Wegh RT, Reid MF, Burdick GW. A complete 4fn energy level diagram for all trivalent lanthanide ions. Journal of Solid State Chemistry. 2005;**178**(2):448-453. DOI: 10.1016/j.jssc.2004.07.046

[7] Solé JG, Bausá LE, Jaque D. An Introduction to the Optical Spectroscopy of Inorganic Solids. 1st ed. Chichester, UK: John Wiley & Sons, Ltd; 2005. 283 p. DOI: 10.1002/0470016043

[8] Yen WM, Shionoya S, Yamamoto H, editors. Practical Applications of Phosphors. 1st ed. Boca Raton, FL: CRC Press; 2006. 528 p.

[9] Dramićanin MD. Sensing temperature via downshifting emissions of lanthanide-doped metal oxides and salts. A review. Methods and Applications in Fluorescence. 2016;**4**(4):42001. DOI: 10.1088/2050-6120/4/4/042001

[10] Eliseeva SV, Bunzli J-CG. Lanthanide luminescence for functional materials and bio-sciences. Chemical Society Reviews. 2010;**39**(1):189-227. DOI: 10.1039/B905604C

[11] Wolfbeis OS. An overview of nanoparticles commonly used in fluorescent bioimaging. Chemical Society Reviews. 2015;**44**(14):4743-4768. DOI: 10.1039/c4cs00392f

[12] Wang Y, He Y, Lai Q, Fan M. Review of the progress in preparing nano TiO_2: An important environmental engineering material. Journal of Environmental Sciences. 2014;**26**(11):2139-2177. DOI: 10.1016/j.jes.2014.09.023

[13] Zhang DR, Jin XZ, Li JH. Effects of Sc and V dopants on the anatase-to-rutile phase transition and crystallite size of TiO_2 nanoparticles. Materials Chemistry and Physics. 2016;**176**:68-74. DOI: 10.1016/j.matchemphys.2016.03.027

[14] Bavykin DV, Friedrich JM, Walsh FC. Protonated titanates and TiO_2 nanostructured materials: Synthesis, properties, and applications. Advanced Materials. 2006;**18**(21):2807-2824. DOI: 10.1002/adma.200502696

[15] Chen X, Mao SS. Titanium dioxide nanomaterials: Synthesis, properties, modifications, and applications. Chemical Reviews. 2007;**107**(7):2891-2959. DOI: 10.1021/cr0500535

[16] Diebold U. The surface science of titanium dioxide. Surface Science Reports. 2003;**48**(5): 53-229. DOI: 10.1016/S0167-5729(02)00100-0.

[17] Roy P, Berger S, Schmuki P. TiO_2 Nanotubes: Synthesis and applications. Angewandte Chemie International Edition. 2011;**50**(13):2904-2939. DOI: 10.1002/anie.201001374

[18] Antić Ž, Krsmanović RM, Nikolić MG, Marinović-Cincović M, Mitrić M, Polizzi S, Dramićanin MD. Multisite luminescence of rare earth doped TiO_2 anatase nanoparticles. Materials Chemistry and Physics. 2012;**135**(2-3):1064-1069. DOI: 10.1016/j.matchemphys.2012.06.016

[19] Luo W, Li R, Liu G, Antonio MR, Chen X. Evidence of trivalent europium incorporated in anatase TiO_2 nanocrystals with multiple sites. The Journal of Physical Chemistry C. 2008;**112**:10370-10377. DOI: 10.1021/jp801563k

[20] Liu Y, Luo W, Zhu H, Chen X. Optical spectroscopy of lanthanides doped in wide band-gap semiconductor nanocrystals. Journal of Luminescence. 2011;**131**(3):415-422. DOI: 10.1016/j.jlumin.2010.07.018

[21] Hanaor DAH, Sorrell CC. Review of the anatase to rutile phase transformation. Journal of Materials Science. 2011;**46**(4):855-874. DOI: 10.1007/s10853-010-5113-0

[22] Baiju KV, Periyat P, Shajesh P, Wunderlich W, Manjumol KA, Smith VS, Jaimy KB, Warrier KGK. Mesoporous gadolinium doped titania photocatalyst through an aqueous sol-gel method. Journal of Alloys and Compounds. 2010;**505**(1):194-200. DOI: 10.1016/j.jallcom.2010.06.028

[23] Shi J-W, Zheng J-T, Wu P. Preparation, characterization and photocatalytic activities of holmium-doped titanium dioxide nanoparticles. Journal of Hazardous Materials. 2009;**161**(1):416-422. DOI: 10.1016/j.jhazmat.2008.03.114

[24] Yurtsever HA, Çiftçioğlu M. The effect of rare earth element doping on the microstructural evolution of sol-gel titania powders. Journal of Alloys and Compounds. 2017;**695**:1336-1353. DOI: 10.1016/j.jallcom.2016.10.275

[25] Nguyen-Phan T-D, Song MB, Kim EJ, Shin EW. The role of rare earth metals in lanthanide-incorporated mesoporous titania. Microporous and Mesoporous Materials. 2009;**119**(1-3):290-298. DOI: 10.1016/j.micromeso.2008.10.039

[26] Liang C-H, Hou M-F, Zhou S-G, Li F-B, Liu C-S, Liu T-X, Gao Y-X, Wang X-G, Lü J-L. The effect of erbium on the adsorption and photodegradation of orange I in aqueous Er^{3+}-TiO_2 suspension. Journal of Hazardous Materials. 2006;**138**(3):471-478. DOI: 10.1016/j.jhazmat.2006.05.066

[27] Milićević B, Đorđević V, Lončarević D, Ahrenkiel SP, Dramićanin MD, Nedeljković JM. Visible light absorption of surface modified TiO_2 powders with bidentate benzene derivatives. Microporous and Mesoporous Materials. 2015;**217**:184-189. DOI: 10.1016/j.micromeso.2015.06.028

[28] Reszczynska J, Grzyb T, Wei Z, Klein M, Kowalska E, Ohtani B, Zaleska-Medynska A. Photocatalytic activity and luminescence properties of RE^{3+}–TiO_2 nanocrystals prepared by sol-gel and hydrothermal methods. Applied Catalysis B: Environmental. 2016;**181**:825-837. DOI: 10.1016/j.apcatb.2015.09.001

[29] Saif M, Abdel-Mottaleb MSA. Titanium dioxide nanomaterial doped with trivalent lanthanide ions of Tb, Eu and Sm: Preparation, characterization and potential applications. Inorganica Chimica Acta. 2007;**360**(9):2863-2874. DOI: 10.1016/j.ica.2006.12.052

[30] Wang R, Wang F, An S, Song J, Zhang Y. Y/Eu co-doped TiO_2: synthesis and photocatalytic activities under UV-light. Journal of Rare Earths. 2015;**33**(2):154-159. DOI: 10.1016/S1002-0721(14)60396-3

[31] Niu X, Li S, Chu H, Zhou J. Preparation, characterization of Y^{3+}-doped TiO_2 nanoparticles and their photocatalytic activities for methyl orange degradation. Journal of Rare Earths. 2011;**29**(3):225-229. DOI: 10.1016/S1002-0721(10)60435-8

[32] Quan X, Zhao Q, Tan H, Sang X, Wang F, Dai Y. Comparative study of lanthanide oxide doped titanium dioxide photocatalysts prepared by coprecipitation and sol-gel process. Materials Chemistry and Physics. 2009;**114**(1):90-98. DOI: 10.1016/j.matchemphys.2008.08.051

[33] Kralova M, Levchuk I, Kasparek V, Sillanpa M, Cihlar J. Influence of synthesis conditions on physical properties of lanthanide-doped titania for photocatalytic decomposition of metazachlor. Chinese Journal of Catalysis. 2015;**36**:1679-1685. DOI: 10.1016/S1872-2067(15)60943-3

[34] Luo W, Li R, Chen X. Host-sensitized luminescence of Nd^{3+} and Sm^{3+} ions incorporated in anatase titania nanocrystals. The Journal of Physical Chemistry C. 2009;**113**(20):8772-8777. DOI: 10.1021/jp901862k

[35] Hu L, Song H, Pan G, Yan B, Qin R, Dai Q, Fan L, Li S, Bai X. Photoluminescence properties of samarium-doped TiO_2 semiconductor nanocrystalline powders. Journal of Luminescence. 2007;**127**(2):371-376. DOI: 10.1016/j.jlumin.2007.01.020

[36] Shi J-W, Zheng J-T, Hu Y, Zhao Y-C. Influence of Fe^{3+} and Ho^{3+} co-doping on the photocatalytic activity of TiO_2. Materials Chemistry and Physics. 2007;**106**(2-3):247-249. DOI: 10.1016/j.matchemphys.2007.05.042

[37] Zhang DR, Liu HL, Han SY, Piao WX. Synthesis of Sc and V-doped TiO_2 nanoparticles and photodegradation of rhodamine-B. Journal of Industrial and Engineering Chemistry. 2013;**19**(6):1838-1844. DOI: 10.1016/j.jiec.2013.02.029

[38] de la Cruz D, Arévalo JC, Torres G, Bautista Margulis RG, Ornelas C, Aguilar-Elguézabal A. TiO_2 doped with Sm^{3+} by sol-gel: Synthesis, characterization and photocatalytic activity of diuron under solar light. Catalysis Today. 2011;**166**(1):152-158. DOI: 10.1016/j.cattod.2010.08.023

[39] Chen D, Zhu Q, Lv Z, Deng X, Zhou F, Deng Y. Microstructural and photocatalytic properties of Eu-doped mesoporous titanium dioxide nanoparticles by sol-gel method. Materials Research Bulletin. 2012;**47**:3129-3134. DOI: 10.1016/j.materresbull.2012.08.021

[40] Ghigna P, Speghini A, Bettinelli M. "Unusual Ln^{3+} substitutional defects": The local chemical environment of Pr^{3+} and Nd^{3+} in nanocrystalline TiO_2 by Ln–K edge EXAFS. Journal of Solid State Chemistry. 2007;**180**(11):3296-3301. DOI: 10.1016/j.jssc.2007.09.025

[41] Huang C., You W, Dang L, Lei Z, Sun Z, Zhang L. Effect of Nd^{3+} doping on photocatalytic activity of TiO_2 nanoparticles for water decomposition to hydrogen. Chinese Journal of Catalysis. 2006;**27**(3):203-209. DOI: 10.1016/S1872-2067(06)60013-2

[42] Bettinelli M, Speghini A, Falcomer D, Daldosso M, Dallacasa V, Romanò L. Photocatalytic, spectroscopic and transport properties of lanthanide-doped TiO_2 nanocrystals. Journal of Physics: Condensed Matter. 2006;**18**:S2149–S2160. DOI: 10.1088/0953-8984/18/33/S30

[43] Hamza MA, Khalil ASh, Yaseen HM. Synthesis of Yb^{3+} doped TiO_2 nano particles powder as IR filter via sol-gel. Advances in Materials Physics and Chemistry. 2013;**3**:214-216. DOI: 10.4236/ampc.2013.34032

[44] Zhang Z, Li G, Cui Z, Zhang K, Feng Y, Meng S. Influence of difference quantity La-doped TiO_2 photoanodes on the performance of dye-sensitized solar cells: A strategy for choosing an appropriate doping quantity. Journal of Solid State Chemistry. 2016;**237**:242-247. DOI: 10.1016/j.jssc.2016.02.005

[45] Li H, Zheng K, Sheng Y, Song Y, Zhang H, Huang J, Huo Q, Zou H. Facile synthesis and luminescence properties of TiO_2:Eu^{3+} nanobelts. Optics and Laser Technology. 2012;**49**:33-37. DOI: 10.1016/j.optlastec.2012.12.007

[46] Zhou W, He Y. Ho/TiO_2 nanowires heterogeneous catalyst with enhanced photocatalytic properties by hydrothermal synthesis method. Chemical Engineering Journal. 2012;**179**:412-416. DOI: 10.1016/j.cej.2011.10.094

[47] Khan M, Cao W. Cationic (V, Y)-codoped TiO_2 with enhanced visible light induced photocatalytic activity: A combined experimental and theoretical study. Journal of Applied Physics. 2013;**114**:183514-1 (7pp). DOI: 10.1063/1.4831658

[48] Bhethanabotla VC, Russell DR, Kuhn JN. Assessment of mechanisms for enhanced performance of Yb/Er/titania photocatalysts for organic degradation: Part 2. Role of rare earth elements in the titania phase. Applied Catalysis B: Environmental. 2017;**202**:156-164. DOI: 10.1016/j.apcatb.2016.09.008

[49] Obregón S, Kubacka A, Fernández-García M, Colón G. High-performance Er^{3+}–TiO_2 system: Dual up-conversion and electronic role of the lanthanide. Journal of Catalysis. 2013;**299**:298-306. DOI: 10.1016/j.jcat.2012.12.021

[50] Pedroni M, Piccinelli F, Polizzi S, Speghini A, Bettinelli M, Haro-González P. Upconverting Ho–Yb doped titanate nanotubes. Materials Letters. 2012;**80**:81-83. DOI: 10.1016/j.matlet.2012.04.096

[51] Yan X, He J, Evans DG, Duan X, Zhu Y. Preparation, characterization and photocatalytic activity of Si-doped and rare earth-doped TiO_2 from mesoporous precursors. Applied Catalysis B: Environmental. 2005;**55**(4):243-252. DOI: 10.1016/j.apcatb.2004.08.014

[52] Qi X, Zou H, Song Y, Zhang H, Zhao H, Shi Z, Sheng Y. Hydrothermal synthesis and luminescence properties of TiO_2: Eu^{3+} submicrospheres. Ceramics International. 2014;**40**:12993-12997. DOI: 10.1016/j.ceramint.2014.04.162

[53] Li H, Sheng Y, Zhao H, Song Y, Gao F, Huo Q, Zou H. Facile synthesis and luminescent properties of TiO_2:Eu^{3+} nanorods and spindle-shaped nanoparticles from titanate nanotubes precursors. Materials Research Bulletin. 2012;**47**(12):4322-4328. DOI: 10.1016/j.materresbull.2012.09.010

[54] Falcomer D, Daldosso M, Cannas C, Musinu A, Lasio B, Enzo S, Speghini A, Bettinelli M. A one-step solvothermal route for the synthesis of nanocrystalline anatase TiO_2 doped with lanthanide ions. Journal of Solid State Chemistry. 2006;**179**(8):2452-2457. DOI: 10.1016/j.jssc.2006.04.043

[55] Wang Y, Chen G, Shen Q, Yang H, Li L, Song Y. A hydrothermal synthesis of Pr^{3+} doped mesoporous TiO_2 for UV light photocatalysis. Journal of Nanoscience and Nanotechnology. 2014;**14**(7):4988-4994. DOI: 10.1166/jnn.2014.9487

[56] Diamandescu L, Vasiliu F, Tarabasanu-Mihaila D, Feder M, Vlaicu AM, Teodorescu CM, et al. Structural and photocatalytic properties of iron- and europium-doped TiO_2 nanoparticles obtained under hydrothermal conditions. Materials Chemistry and Physics. 2008;**112**(1):146-153. DOI: 10.1016/j.matchemphys.2008.05.023

[57] Cacciotti I, Bianco A, Pezzotti G, Gusmano G. Synthesis, thermal behaviour and luminescence properties of rare earth-doped titania nanofibers. Chemical Engineering Journal. 2011;**166**(2):751-764. DOI: 10.1016/j.cej.2010.07.008

[58] Hassan MS, Amna T, Yang O-B, Kim H-C, Khil M-S. TiO_2 nanofibers doped with rare earth elements and their photocatalytic activity. Ceramics International. 2012;**38**(7):5925-5930. DOI: 10.1016/j.ceramint.2012.04.043

[59] Kumar KS, Song C-G, Bak GM, Heo G, Seong M-J, Yoon J-W. Phase control of yttrium (Y)-doped TiO_2 nanofibers and intensive visible photoluminescence. Journal of Alloys and Compounds. 2014;**617**:683-687. DOI: 10.1016/j.jallcom.2014.08.067

[60] Cacciotti I, Bianco A, Pezzotti G, Gusmano G. Terbium and ytterbium-doped titania luminescent nanofibers by means of electrospinning technique. Materials Chemistry and Physics. 2011;**126**(3):532-541. DOI: 10.1016/j.matchemphys.2011.01.034

[61] Yang Y, Zhang C, Xu Y, Wang H, Li X, Wang C. Electrospun Er:TiO_2 nanofibrous films as efficient photocatalysts under solar simulated light. Materials Letters. 2010;**64**(2):147-150. DOI: 10.1016/j.matlet.2009.10.028

[62] Ikeda M, Li J-G, Kobayashi N, Moriyoshi Y, Hamanaka H, Ishigaki T. Phase formation and luminescence properties in Eu^{3+}-doped TiO_2 nanoparticles prepared by thermal plasma pyrolysis of aqueous solutions. Thin Solid Films. 2008;**516**(19):6640-6644. DOI: 10.1016/j.tsf.2007.11.037

[63] Liu H, Yu L, Chen W, Li Y. The progress of TiO_2 nanocrystals doped with rare earth ions. Journal of Nanomaterials. 2012;**2012**:235879. DOI: 10.1155/2012/235879

[64] Mazierski P, Lisowski W, Grzyb T, Winiarski MJ, Klimczuk T, Mikołajczyk A, et al. Enhanced photocatalytic properties of lanthanide-TiO_2 nanotubes: An experimental and theoretical study. Applied Catalysis B: Environmental. 2017;**205**:376-385. DOI: 10.1016/j.apcatb.2016.12.044

[65] Cheng XQ, Ma CY, Yi XY, Yuan F, Xie Y, Hu JM, Hu BC, Zhang QY. Structural, morphological, optical and photocatalytic properties of Gd-doped TiO_2 films. Thin Solid Films. 2016;**615**:13-18. DOI: 10.1016/j.tsf.2016.06.049

[66] Borlaf M, Caes S, Dewalque J, Colomer MT, Moreno R, Cloots R, Boschini F. Effect of the RE (RE = Eu, Er) doping on the structural and textural properties of mesoporous TiO_2 thin films obtained by evaporation induced self-assembly method. Thin Solid Films. 2014;**558**:140-148. DOI: 10.1016/j.tsf.2014.03.002

[67] Conde-Gallardo A, Garciá-Rocha M, Hernández-Calderón I, Palomino-Merino R. Photoluminescence properties of the Eu^{3+} activator ion in the TiO_2 host matrix. Applied Physics Letters. 2001;**78**(22):3436-3438. DOI: 10.1063/1.1372338

[68] Burns A, Hayes G, Li W, Hirvonen J, Demaree JD, Shah SI. Neodymium ion dopant effects on the phase transformation in sol-gel derived titania nanostructures. Materials Science and Engineering B. 2004;**111**:150-155. DOI: 10.1016/j.mseb.2004.04.008

[69] Meng Q, Zhang H, Wang S, Fu L, Zheng Y, Yang K. Preparation and characterization of luminescent thin films doped with rare earth (Tb^{3+}, Eu^{3+}) complexes derived from a sol-gel process. Materials Letters. 2000;**45**:213-216. DOI: 10.1016/S0167-577X(00)00107-5

[70] Zhang J, Li M, Feng Z, Chen J, Li C. UV Raman spectroscopic study on TiO_2. I. Phase transformation at the surface and in the bulk. The Journal of Physical Chemistry B. 2006;**110**:927-935. DOI: 10.1021/jp0552473

[71] Zhang Y, Zhang H, Xu Y, Wang Y. Europium doped nanocrystalline titanium dioxide: Preparation, phase transformation and photocatalytic properties. Journal of Materials Chemistry. 2003;**13**:2261-2265. DOI: 10.1039/b305538h

[72] Stengl V, Bakardjieva S. Molybdenum-doped anatase and its extraordinary photocatalytic activity in the degradation of orange II in the UV and Vis regions. The Journal of Physical Chemistry C. 2010;**114**(45):19308-19317. DOI: 10.1021/jp104271q

[73] Li F, Li X, Hou M. Photocatalytic degradation of 2-mercaptobenzothiazole in aqueous La^{3+}–TiO_2 suspension for odor control. Applied Catalysis B: Environmental. 2004;**48**(3):185-194. DOI: 10.1016/j.apcatb.2003.10.003

[74] Parida KM, Sahu N. Visible light induced photocatalytic activity of rare earth titania nanocomposites. Journal of Molecular Catalysis A: Chemical. 2008;**287**(1-2):151-158. DOI: 10.1016/j.molcata.2008.02.028

[75] El-Bahy ZM, Ismail AA, Mohamed RM. Enhancement of titania by doping rare earth for photodegradation of organic dye (Direct Blue). Journal of Hazardous Materials. 2009;**166**:138-143. DOI: 10.1016/j.jhazmat.2008.11.022

[76] Serp P, Machado B. Photocatalysis on nanostructured carbon supported catalysts. In: Nanostructured Carbon Materials for Catalysis. Great Britain:The Royal Society of Chemistry; 2015. pp. 412-444. DOI: 10.1039/9781782622567-00412

[77] Xie Y, Yuan C. Photocatalysis of neodymium ion modified TiO_2 sol under visible light irradiation. Applied Surface Science. 2004;**221**:17-24. DOI: 10.1016/S0169-4332(03)00945-0

[78] Xu A-W, Gao Y, Liu H-Q. The preparation, characterization, and their photocatalytic activities of rare-earth-doped TiO_2 nanoparticles. Journal of Catalysis. 2002;**207**:151-157. DOI: 10.1006/jcat.2002.3539

[79] Hörmann U, Kaiser U, Albrecht M, Geserick J, Hüsing N. Structure and luminescence of sol-gel synthesized anatase nanoparticles. Journal of Physics: Conference Series. 2010;**209**(1):012039 (7pp). DOI: 10.1088/1742-6596/209/1/012039

[80] Yang J, Dai J, Li J. Synthesis, characterization and degradation of bisphenol A using Pr, N co-doped TiO_2 with highly visible light activity. Applied Surface Science. 2011;**257**(21):8965-8973. DOI: 10.1016/j.apsusc.2011.05.074

[81] Su W, Chen J, Wu L, Wang X, Wang X, Fu X. Visible light photocatalysis on praseodymium(III)-nitrate-modified TiO_2 prepared by an ultrasound method. Applied Catalysis B: Environmental. 2008;**77**:264-271. DOI: 10.1016/j.apcatb.2007.04.015

[82] Li Y-C, Chang Y-H, Lin Y-F, Chang Y-S, Lin Y-J. Luminescent properties of trivalent praseodymium-doped lanthanum aluminum germanate LaAlGe2O7. Journal of Physics and Chemistry of Solids. 2007;**68**(10):1940-1945. DOI: 10.1016/j.jpcs.2007.06.013

[83] de Sousa Filho PC, Lima JF, Serra OA. From lighting to photoprotection: Fundamentals and applications of rare earth materials. Journal of the Brazilian Chemical Society. 2015;**26**(12):2471-2495. DOI: 10.5935/0103-5053.20150328

[84] Yildirim S, Yurddaskal M, Dikici T, Aritman I, Ertekin K, Celik E. Structural and luminescence properties of undoped, Nd^{3+} and Er^{3+} doped TiO_2 nanoparticles synthesized by flame spray pyrolysis method. Ceramics International. 2016;**42**(9):10579-10586. DOI: 10.1016/j.ceramint.2016.03.131

[85] Dolgov L, Kiisk V, Reedo V, Pikker S, Sildos I, Kikas J. Sensitizing of Sm^{3+} fluorescence by silver dopant in the TiO_2 films. Central European Journal of Physics. 2011;**9**(2):542-546. DOI: 10.2478/s11534-010-0069-x

[86] Buenzli JCG, Plancherel D, Pradervand GO. The europium(III) ion as luminescent probe: structural investigation of complexes between europium nitrate and two polyethers. The Journal of Physical Chemistry. 1989;**93**(2):980-984. DOI: 10.1021/j100339a083

[87] Wolfbeis OS, Dürkop A, Wu M, Lin Z. A europium-ion-based luminescent sensing probe for hydrogen peroxide. Angewandte Chemie International Edition. 2002;**41**(23):4495-4498. DOI: 10.1002/1521-3773(20021202)41:23<4495::AID-ANIE4495>3.0.CO;2-I

[88] Reisfeld R, Zigansky E, Gaft M. Europium probe for estimation of site symmetry in glass films, glasses and crystals. Molecular Physics. 2004;**102**(11-12):1319-1330. DOI: 10.1080/00268970410001728609

[89] Tanner PA. Some misconceptions concerning the electronic spectra of tri-positive europium and cerium. Chemical Society Reviews. 2013;**42**(12):5090-5101. DOI: 10.1039/C3CS60033E

[90] Binnemans K. Interpretation of europium(III) spectra. Coordination Chemistry Reviews. 2015;**295**:1-45. DOI: 10.1016/j.ccr.2015.02.015

[91] Xueyuan C, Wenqin L, Yongsheng L, Guokui L. Recent progress on spectroscopy of lanthanide ions incorporated in semiconductor nanocrystals. Journal of Rare Earths. 2007;**25**(5):515-525. DOI: 10.1016/S1002-0721(07)60555-9

[92] Chakraborty A, Debnath GH, Saha NR, Chattopadhyay D, Waldeck DH, Mukherjee P. Identifying the correct host-guest combination to sensitize trivalent lanthanide (guest) luminescence: Titanium dioxide nanoparticles as a model host system. The Journal of Physical Chemistry C. 2016;**120**(41):23870-23882. DOI: 10.1021/acs.jpcc.6b08421